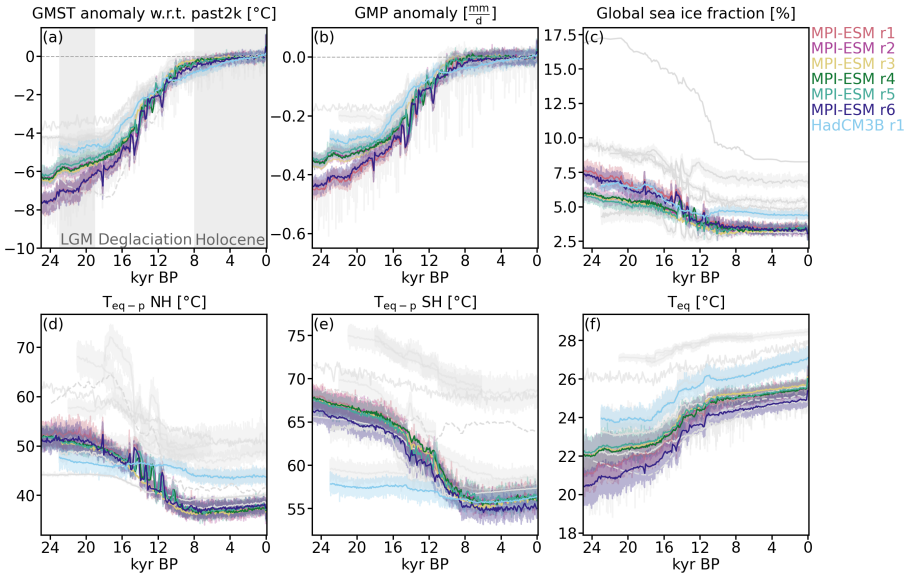

Figure S1. Centennial mean climate variables for the sensitivity set (MPI-ESM r1–r6 and HadCM3B r1) from LGM to Holocene with annual data as shading. The main set is shaded in gray and shown in Fig. 2. (a) GMT and (b) GMP anomaly with respect to the past 2 kyr. (c) Global sea ice fraction. (d, e) Equator-to-pole temperature difference for the Northern and Southern Hemisphere respectively, computed as the difference between the polar (70°-90°) and equatorial temperatures (15°S-15°N). The latter are shown in (f).

1 Supplementary Material

S1 Main and sensitivity set of simulations

Fig. S1 shows the features of main climate of the sensitivity set analogous to Fig. 2 in the main text.

S2 simulation exploration

S2.1 The TransEBM Deglacial simulation

Using TransEBM (Ziegler and Rehfeld, 2021), we simulate the linear climate response to the forcings of the last 26k years. The first 25 years of the simulation serve as spin up. The model computes the orbital parameters following Berger (1978). Annual incoming solar radiation is constructed as a surrogate forcing based on a 9300 yr reconstruction of Holocene total solar irradiance by Steinhilber et al. (2009). From this reconstruction, we construct several artifical timeseries using the Amplitude Adjusted Fourier transform surrogate method with random seeds (Theiler et al., 1992) following Ellerhoff and Rehfeld (2021) to construct a forcing timeseries (Fig. S2). As greenhouse gas forcing, the simulation uses the reconstruction of CO_2 by Köhler et al. (2017). Like MPI-ESM r7, it employs the volcanic forcing PalVol V.1 (Schindlbeck-Belo et al., 2023). TransEBM employs it as an annual averaged volcanic forcing, which we regridded using linear interpolation and then applied to 2.8° wide latitudinal bands. Changes to the land sea mask and ice sheets follow ICE6G (Peltier et al., 2015). Since changes in the EBM produce an immediate climate response we interpolate the ice sheets during periods of rapid sea level rise to simulate a more gradual change in ice sheet cover. To this end, we identify areas of land ice, which change between consecutive reconstructions. In these places, ice is gradually removed with sea level change, starting from grid cells closer to equator. At the same latitude ice at places with smaller longitude is removed first. As a result, land ice cover changes in the simulation at intervals between 125 to 500 yr. Sea ice is also modelled as a surface type with specific properties (heat capacity and albedo). As such, it serves as

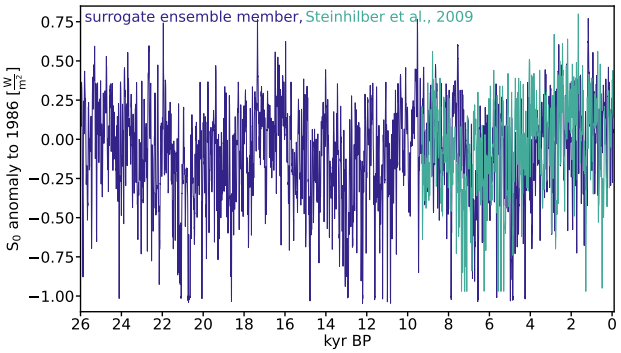

Figure S2. Comparison of the solar forcing reconstruction of Steinhilber et al. (2009) with one ensemble member generated as surrogate data based on it following (Ellerhoff and Rehfeld, 2021).

an external forcing in the simulation. We construct it by interpolating between LGM and present-day distributions by (Zhuang et al., 2017) with the same method as for land ice. To mimic freshwater induced variability in the North Atlantic heat transport, we modulate the North Atlantic heat diffusivity in the model to match SST reconstructions by (Jonkers et al., 2020).

S2.2 Axes of the model hierarchy

The hierarchy constructed in Sect. 2.1.1 and Fig. 3a includes eight axis: the resolution of atmosphere and ocean, the atmosphere and ocean model, the bands of long- and shortwave radiation, land hydrology, vegetation and aerosols. Resolution does not necessarily equal complexity. Increased resolution can however hold a larger potential for more complex simulated dynamics. For long transient simulations, computational demand limits resolution. Within those limits our analysis contains simulations with horizontal resolutions ranging from 48×37 and T21 to T42 in the atmosphere and from $3.75° \times 2.5°$ to $1.25° \times 1.25°$ in the ocean. Vertical layers in the atmosphere range from none in the case of TransEBM, 3 as the smallest amount of vertical layers in ECBilt to 31 in MPI-ESM. For the ocean, vertical layers are either again none for the EBM, 20 or 40. To summarize these differences in resolution for the hierarchy, atmospheric resolution is ranked by the amount of grid boxes computed as horizontal resolution times vertical resolution. For the ocean model resolution, horizontal and vertical resolution are ranked separately and then the average is taken for the hierarchy. This approach was chosen to be able to account for the variable latitudinal resolution that gets finer towards the equator in TraCE-21ka. Regarding the atmospheric resolution, the EBM and ECBilt make up the lowest tier, FAMOUS is ranked one above and the other GCMs and ESMs constitute the highest tier, mirroring the traditional hierarchy from EBM and EMIC to ESMs. For the oceanic resolution, the picture is more varied as CLIO has a higher resolution and complexity then the atmospheric model ECBilt it is coupled to. As a result, its resolution is larger than that of the ocean models in TraCE-21ka and FAMOUS. The resolution of HadCM3B is larger still and MPI-ESM has the largest oceanic resolution in found in this study. The EBM models the ocean as a surface type and thus ranks as zero.

Overall, the resolutions of all simulations remain limited so as to enable the transient modeling of the Last Deglaciation. However, how much such limited resolutions impacts the simulated climate and thus its study can be unclear. While an increase in resolution allows to better resolve topographic features and can lead to improved representation of regional phenomena and circulation patterns (Liu et al., 2022; Schiemann et al., 2014; Roeckner et al., 2006; Paolini et al., 2022; Kirtman et al., 2012), higher resolution does not always translate to large changes in the simulated climate. However, many of these studies see benefits when hitherto parameterized climatic features can be resolved, e.g. in convection- or eddy-resolving simulations. Otherwise, for many climatic features, the effect of increasing spatial resolution on the ability of simulations to reproduce observations can be smaller than expected. All in all, the resolutions of the simulations considered here thus allow for the study of global climate and its evolution since the LGM.

For the atmosphere model, the hierarchy considers the following options: 0D point model, 1D model (both not represented in this study), 2D model (TransEBM), 3D (quasi-)geostrophic (ECBilt), primitive equations (all others) and could further

extend to modeling of non-hydrostatic equations and full Navier-Stokes equations. We further distinguish the radiative models in the atmospheric model by the total number of long- and shortwave radiative bands, which range from $1+1$ (TransEBM, ECBilt), $6+8$ (FAMOUS, HadCM3B) and $19+8$ (TraCE-21ka) to $14+16$ (MPI-ESM). Regarding the ocean model, many options exist, of which the simulations included here only cover a few: prescribed surface type/ no ocean model (TransEBM), an ocean component with primitive equations with (FAMOUS, HadCM3B) and without (CLIO, TraCE-21ka, MPI-ESM) a rigid lid approximation. The simulations do not include options such as prescribed SSTs, a slab or geostrophic ocean, although they are included in the hierarchy in theory. The land hydrology options range from none (TransEBM), to a single layer with a bucket model (LOVECLIM simulations) and multi-layer models (FAMOUS, HadCM3B, TraCE-21ka), which can include a river-routing model (MPI-ESM). For vegetation, the options are prescribed (TransEBM, LOVECLIM simulations), models with a terrestrial carbon cycle (not included), dynamic vegetation models (FAMOUS, HadCM3B, TraCE-21ka) and a dynamic vegetation model that includes a nitrogen cycle (MPI-ESM). Lastly, the inclusion of aerosols varies from none at all (TransEBM, LOVECLIM simulations), to prescribed (FAMOUS, HadCM3B), modeling of sulfates (TraCE-21ka) and other aerosols in addition to sulfates, e.g. NH_3 (MPI-ESM).

S3 Supplements to the methods section

Figure S3 compares different versions of detrending. Among others, it shows the results when using linear detrending with breakpoints at the transitions from LGM to Deglaciation (19kyr BP) and Deglaciation to Holocene (8kyr BP). Different kernel sizes for the Gaussian smoothing are compared as well, from $\sigma = 1000\,\mathrm{yr}$ to the $4000\,\mathrm{yr}$ used for the main manuscript. Linear detrending is the only method that produces notably different results and clear artifacts, e.g. in panels g, k, u and w. While the different kernel sizes produce differences mostly during times of abrupt changes, which will be removed as trend rather than variability as the kernel size gets smaller and thus closer to the timescale of these changes.

Figure S4 shows example timeseries as drawn from the distributions shown in Fig. 4. The timeseries thus demonstrate the potential effects of differences in one or several moments.

S4 Moments per simulations

S4.1 Global mean moments

Figures S5 and S6 show the global mean moments from LGM to Holocene for surface temperature and precipitation by complexity category. Figure S7 shows the same split by individual models simulations. Tables Table S1 and S2 list the LGM-to-Holocene changes in moments per simulations, which are summarized per complexity category in Table 2 of the main text.

S4.2 Zonal moments

Figures S8 and S9 complement Fig. 5 in the main text and show the latitudinal profiles of the moments for the individual simulations. Figure S10 further highlights the changes with background state from LGM to Deglaciation to Holocene.

S4.3 Moments in space

To highlight the differences with timescale, we here show the moments in space according to timescale that are not included in the main text. Figure S11 first shows the mean changes of both surface temperature and precipitation for three examples simulations — MPI-ESM r7, TraCE-21ka and ECBilt-CLIO — and reveals the simulated global warming and wetting from LGM to Holocene across the ensemble. Figure S12 shows the spatial patterns of the higher order moments on centennial scales for the same example simulations for surface temperature. Figures S13 and S14 show the same for precipitation on centennial and annual timescales, respectively.

To complete the analysis of the effects of forcings on the distributions from the main text, Fig. S15 starts by showing the impacts of forcings on annual standard deviation of surface temperature. Further Fig. S16 and S17 display the same for decadal

Table S1. LGM to Holocene changes in the moments of surface temperature for all simulations and timescales. For the mean, the absolute value of the difference is listed, for the other moments the ratios.

	$\Delta m_{hol-lgm}$	v_{lgm}/v_{hol}			s_{lgm}/s_{hol}			k_{lgm}/k_{hol}		
	T	T_{ann}	T_{dec}	T_{cen}	T_{ann}	T_{dec}	T_{cen}	T_{ann}	T_{dec}	T_{cen}
MPI-ESM ch4	4.41	1.63	1.49	2.05	4.60	9.26	0.27	0.77	0.14	-0.01
MPI-ESM r1	6.51	1.97	1.69	2.38	-1.43	-0.09	-0.09	0.30	0.02	0.04
MPI-ESM r2	5.52	1.51	1.00	0.92	-1.39	-0.04	-0.04	0.49	0.02	-0.01
MPI-ESM r3	5.69			0.81			0.05			-0.01
MPI-ESM r4	5.57			1.07			0.09			-0.01
MPI-ESM r5	5.30	1.49	0.95	0.81	-1.03	-3e-3	0.03	0.35	0.02	-3e-3
MPI-ESM r6	6.48	1.89	1.47	1.44	-1.59	-0.08	0.01	0.30	0.02	0.03
MPI-ESM r7	6.62	2.03	1.97	2.69	1.27	1.52	1.65	0.84	1.35	-2.08
TraCE-21ka	4.11	0.85	0.74	0.63	1.84	-0.20	0.09	0.92	0.10	-0.16
HadCM3B r1	4.45	1.47	1.52	1.95	-7.69	10.61	-3.10	0.84	0.33	-1.20
HadCM3B r2	4.76	1.47	1.49	1.83	-1.86	-0.08	3.36	0.87	0.43	-0.59
FAMOUS	3.07			1.58			2.84			0.96
ECBilt-CLIO	3.95	1.16	1.03	0.74	0.87	0.76	0.84	0.38	0.09	-0.17
TransEBM	4.12	1.27	1.39	1.56	0.90	0.98	-0.01	0.60	0.60	-0.29

Table S2. LGM to Holocene changes in the moments of precipitation for all simulations and timescales. For the mean, the absolute value of the difference is listed, for the other moments the ratios.

	$\Delta m_{hol-lgm}$	v_{lgm}/v_{hol}			s_{lgm}/s_{hol}			k_{lgm}/k_{hol}		
	p	p_{ann}	p_{dec}	p_{cen}	p_{ann}	p_{dec}	p_{cen}	p_{ann}	p_{dec}	p_{cen}
MPI-ESM ch4	0.27	1.23	1.18	1.27	1.16	1.21	2.33	1.60	0.98	0.17
MPI-ESM r1	0.39	1.11	1.05	1.19	1.07	0.98	-0.73	1.03	0.67	0.27
MPI-ESM r2	0.31	1.18	1.11	1.07	1.05	1.00	0.18	1.03	0.72	-0.40
MPI-ESM r3	0.34			0.89			1.12			-0.33
MPI-ESM r4	0.32			1.05			0.36			-0.30
MPI-ESM r5	0.30	1.22	1.10	0.95	1.06	1.02	0.21	0.92	0.73	2e-3
MPI-ESM r6	0.37	1.13	1.08	1.05	1.09	0.94	0.54	1.15	0.65	-0.06
MPI-ESM r7	0.39	1.12	1.09	1.13	1.06	0.95	1.09	0.86	1.11	-1.07
TraCE-21ka	0.20	0.82	0.77	0.57	1.00	0.94	0.76	1.00	0.32	-1.29
HadCM3B r1	0.26	0.82	0.84	0.84	1.12	1.19	1.07	1.88	1.53	-2.56
HadCM3B r2	0.27	0.83	0.86	0.91	1.15	1.28	0.77	2.03	2.08	0.47
FAMOUS	0.15			1.03			1.44			-31.55
ECBilt-CLIO	0.25	0.93	0.93	0.88	1.36	1.33	101.84	1.36	-0.13	-2.44

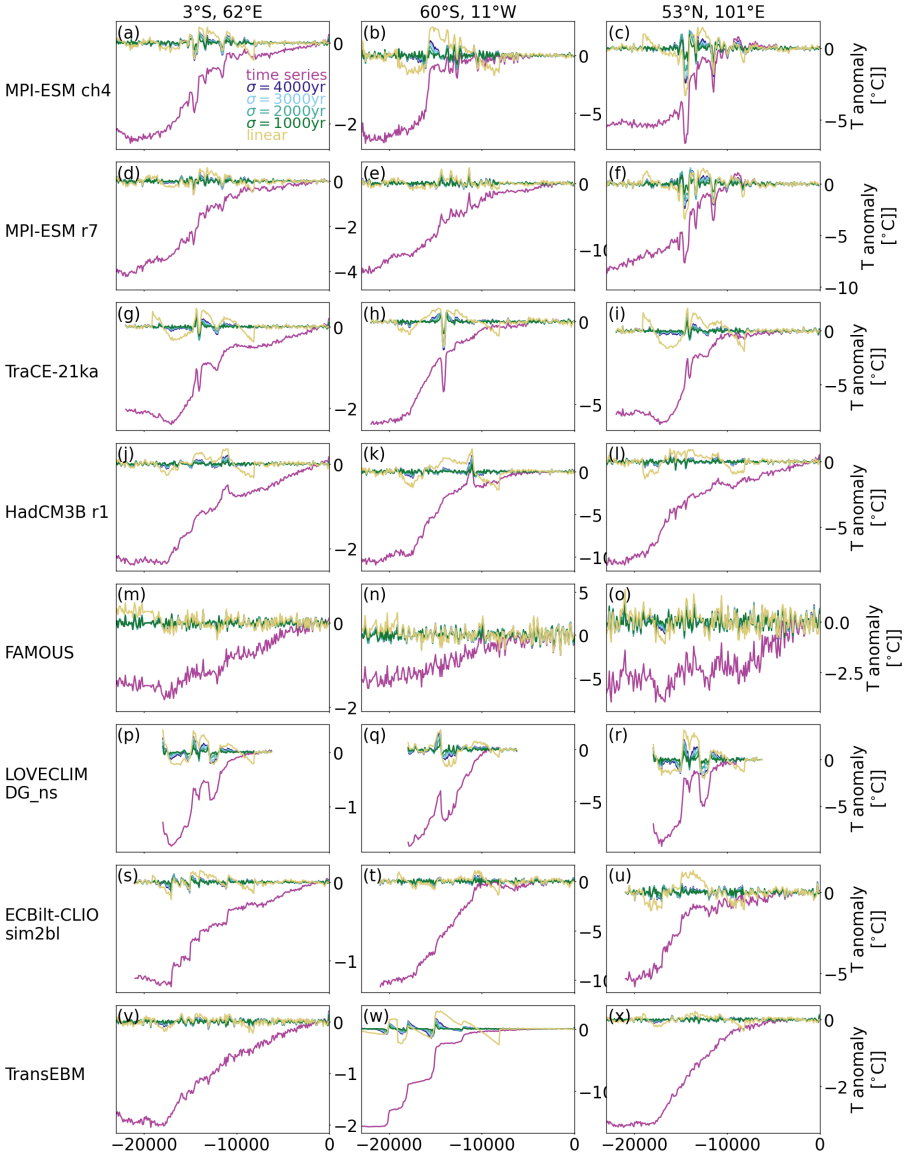

Figure S3. Effects of different versions of detrending on the resulting timeseries used for calculating the moments and spectra in the main text. Shown are different values for the kernel size σ of the Gaussian smoothing, as well as linear detrending with 2 breakpoints.

and annual temperature skewness, while Fig. Fig. S18 and S19 present forcing impacts on decadal and annual temperature kurtosis, respectively. For precipitation, we show decadal (Fig. S20) and annual standard deviation (Fig. S21), decadal (Fig. S22) and annual skewness (Fig. S23), as well as decadal (Fig. S24) and annual kurtosis (Fig. S25). Finally, Fig. S26 presents the spatial changes in mean, standard deviation, skewness and kurtosis for the LGMR.

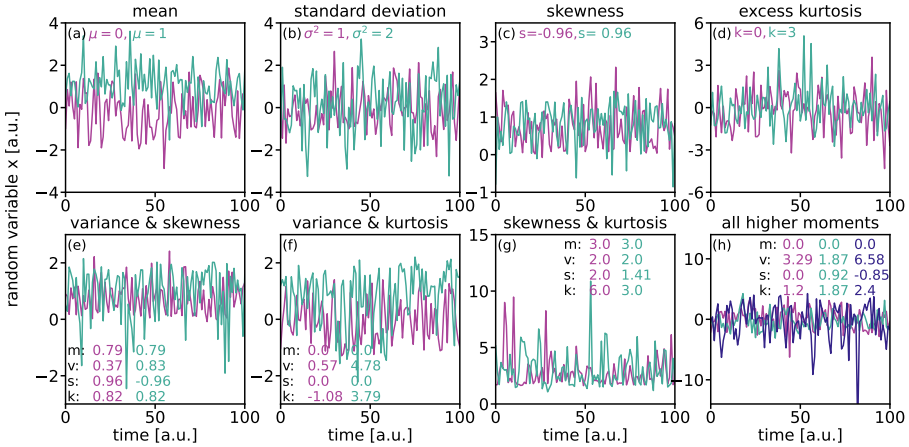

Figure S4. Exemplary timeseries for changes in the moments as sampled from the distributions as shown in Fig. 4. In the upper row only one moment of the corresponding distribution changes, in the bottom row several moments change.

S5 Spectra

Figure S27 shows the global power spectra of the sensitivity set complementing Fig. 12 of the main text, which shows the same for the main set simulations.

S5.1 Regional spectra

Figures S28 (main set) and S29 (sensitivity set) show mean regional temperature spectra for the polar, mid-latitude and tropical regions in the Southern and Northern Hemisphere. Figures S30 and S31 present the same but for precipitation.

S6 Mechanisms

S6.1 Variability of sea ice and its influence on temperature

S6.1.1 Moments of centennial sea ice distributions

To investigate the contribution of sea ice changes to changes in variability, Fig. S32, S33, S34 and S35 show the spatial patterns of change in the moments of sea ice for mean, standard deviation, skewness and kurtosis, respectively.

S6.1.2 Investigation of the 120–320 yr LGM periodicity in MPI-ESM ch4

The spectra of surface temperature and precipitation show a periodicity of roughly 200 years during the LGM in MPI-ESM ch4 that is largest in the high southern latitudes (Fig. 12, S27–S31). A bandbass analysis of standard deviation for timescales from 120–320 years reveals that this originates in the sea ice of the Southern Ocean: MPI-ESM ch4 simulates particularly high standard deviation in the Southern Ocean, with the exception of the Weddel Sea. The standard deviation during the LGM in ch4 is similar or even higher than during the Deglaciation (Fig. S36) and it is larger than in any of the other simulations during the LGM (Fig. S37).

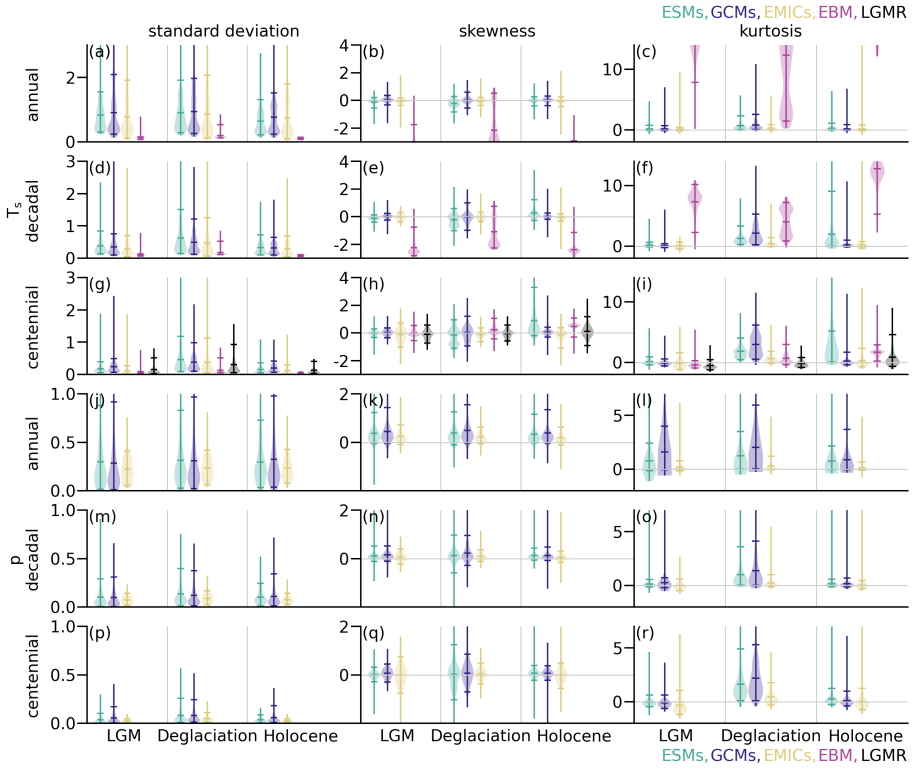

Figure S5. Global annual, decadal and centennial higher order moments of temperature (a-i) and precipitation (j-r). Simulations are summarized by their complexity into ESMs (green), GCMs (blue), EMICs (yellow) and EBM (red) and are shown with the means of the 95th percentiles in space of the individual models. For each moment, standard deviation (left column), skewness (middle column) and kurtosis (right column), results are shown separately for LGM, Deglaciation and Holocene with gray lines separating the periods. Fig. S6 shows the full ranges of all moments and S7 shows the same for all simulations individually. For (c) the 95th percentile of the EBM is cut-off for better comparability of the other moments.

S6.2 Change in temperature gradient

Figure S38 shows the simulated relationships between meridional temperature gradients and LGM-to-Holocene variance ratio for all simulations. While an increased meridional temperature gradient during the LGM has been suggested as a cause for increased LGM variance in comparison to the Holocene, our results cannot confirm this hypothesis.

S7 Robustness tests

To test the robustness of our results, we checked how the regridding, various versions of detrending (see Sec. S3) and the definition of the time periods affect the results. The results from a selection of these tests are shown here by showing the changes in latitudinal moments without regridding and different time period definitions in comparison to the version used in the main text.

We find that the effect of the regridding is negligible for all time periods (Fig. S39–S41). For the definitions of the time periods, we find that extending the LGM up until $18\,\mathrm{kyr}$ BP, results in Deglacial changes being included in the LGM for some of the simulations, but has still mostly limited effects, primarily on kurtosis (e.g. Fig. S39r, t, u). Limiting the LGM to run only up until $20\,\mathrm{kyr}$ BP, on the other hand, means that there is far less data for some simulations, e.g. ECBilt-CLIO (Fig. S39p–r). As

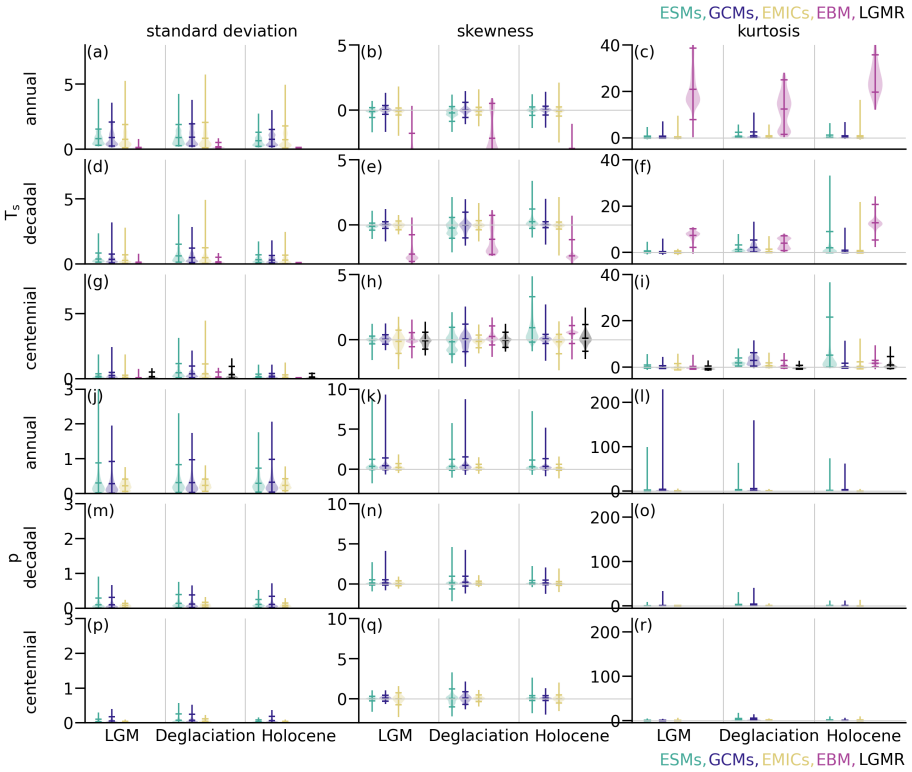

Figure S6. Same as Fig. S5, but showing the full range.

such 19 kyr BP as the end point of the LGM seems suitable, since it ensures enough data points for the computations without including a strong warming trend.

Regarding the definitions of onset and close of the Deglaciation, the general patterns hold when these are changed (S40). The largest differences can be found for kurtosis, but the degree of change differs between simulations. There is a similar ranking in overall levels of variability among most of the models: 20–8 > 20–9 & 19–8 > 20–10 & 19–9 > 19–10 kyr BP. An earlier onset and close thus tend to lead to slightly higher kurtosis. However, the differences do not impact any of the conclusions drawn in the main text.

For the Holocene, too, a changing onset mostly has small impacts, primarily on kurtosis (Fig.)S41). For some simulations starting at 10 kyr, and sometimes even 9 kyr, means that the end of Deglaciation is included in the Holocene (e.g. in MPI-ESM r7), impacting moments in high latitudes and especially the Northern Hemisphere. This is most notable for TransEBM (panels v–x). Overall, we find limited effects from both regridding and the definitions of LGM, Deglaciation and Holocene on the results. Where they exist, these are limited to kurtosis and change the overall levels of kurtosis slightly but not the patterns.

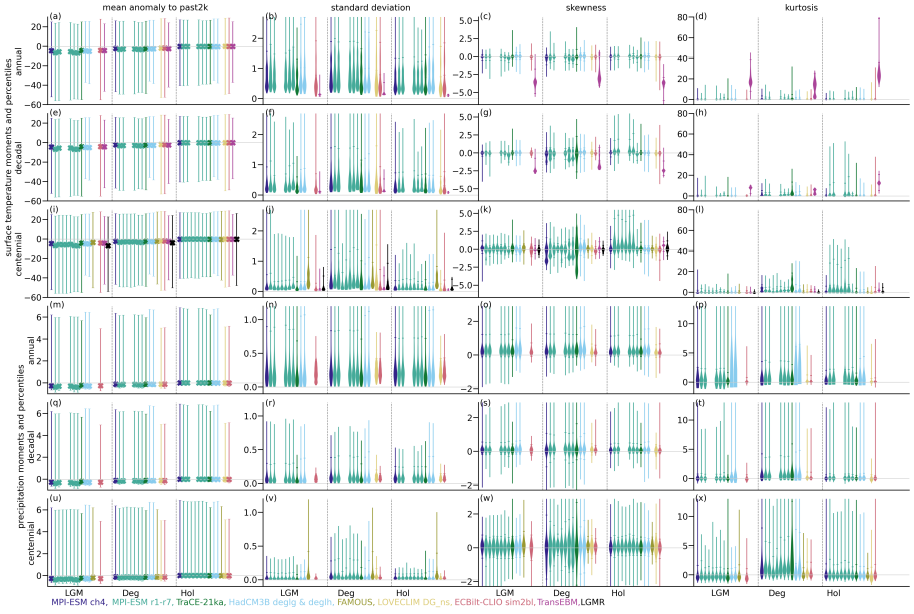

Figure S7. Global annual, decadal and centennial moments of temperature (a-l) and precipitation (k-x) as in Fig. S5 but for all simulations. Simulations are shown with the means of the 95th percentiles in space of the individual models. For each moment, mean (first column), standard deviation (second column), skewness (third column) and kurtosis (fourth column), results are shown separately for LGM, Deglaciation and Holocene with gray lines separating the periods.

References

Berger, A. L.: Long-Term Variations of Daily Insolation and Quaternary Climatic Changes, Journal of the Atmospheric Sciences, 35, 2362–2367, https://doi.org/10.1175/1520-0469(1978)035<2362:LTVODI>2.0.CO;2, 1978.

Ellerhoff, B. and Rehfeld, K.: Probing the Timescale Dependency of Local and Global Variations in Surface Air Temperature from Climate Simulations and Reconstructions of the Last Millennia, Physical Review E, 104, 1–14, https://doi.org/10.1103/PhysRevE.104.064136, 2021.

Jonkers, L., Cartapanis, O., Langner, M., McKay, N., Mulitza, S., Strack, A., and Kucera, M.: Integrating Palaeoclimate Time Series with Rich Metadata for Uncertainty Modelling: Strategy and Documentation of the PALMOD 130k Marine Palaeoclimate Data Synthesis, Earth System Science Data Discussions, 908831, 1–53, https://doi.org/10.5194/essd-2019-223, 2020.

Kirtman, B. P., Bitz, C., Bryan, F., Collins, W., Dennis, J., Hearn, N., Kinter, J. L., Loft, R., Rousset, C., Siqueira, L., Stan, C., Tomas, R., and Vertenstein, M.: Impact of Ocean Model Resolution on CCSM Climate Simulations, Climate Dynamics, 39, 1303–1328, https://doi.org/10.1007/s00382-012-1500-3, 2012.

Köhler, P., Nehrbass-Ahles, C., Schmitt, J., Stocker, T. F., and Fischer, H.: A 156 Kyr Smoothed History of the Atmospheric Greenhouse Gases CO2, CH4, and N2O and Their Radiative Forcing, Earth System Science Data, 9, 363–387, https://doi.org/10.5194/essd-9-363-2017, 2017.

Liu, B., Gan, B., Cai, W., Wu, L., Geng, T., Wang, H., Wang, S., Jing, Z., and Jia, F.: Will Increasing Climate Model Resolution Be Beneficial for ENSO Simulation?, Geophysical Research Letters, 49, e2021GL096 932, https://doi.org/10.1029/2021GL096932, 2022.

Paolini, L. F., Athanasiadis, P. J., Ruggieri, P., and Bellucci, A.: The Atmospheric Response to Meridional Shifts of the Gulf Stream SST Front and Its Dependence on Model Resolution, Journal of Climate, 35, 6007–6030, https://doi.org/10.1175/JCLI-D-21-0530.1, 2022.

Peltier, W. R., Argus, D. F., and Drummond, R.: Space Geodesy Constrains Ice Age Terminal Deglaciation: The Global ICE-6G_C (VM5a) Model, Journal of Geophysical Research: Solid Earth, 120, 450–487, https://doi.org/10.1002/2014JB011176, 2015.

Roeckner, E., Brokopf, R., Esch, M., Giorgetta, M., Hagemann, S., Kornblueh, L., Manzini, E., Schlese, U., and Schulzweida, U.: Sensitivity of Simulated Climate to Horizontal and Vertical Resolution in the ECHAM5 Atmosphere Model, Journal of Climate, 19, 3771–3791, https://doi.org/10.1175/JCLI3824.1, 2006.

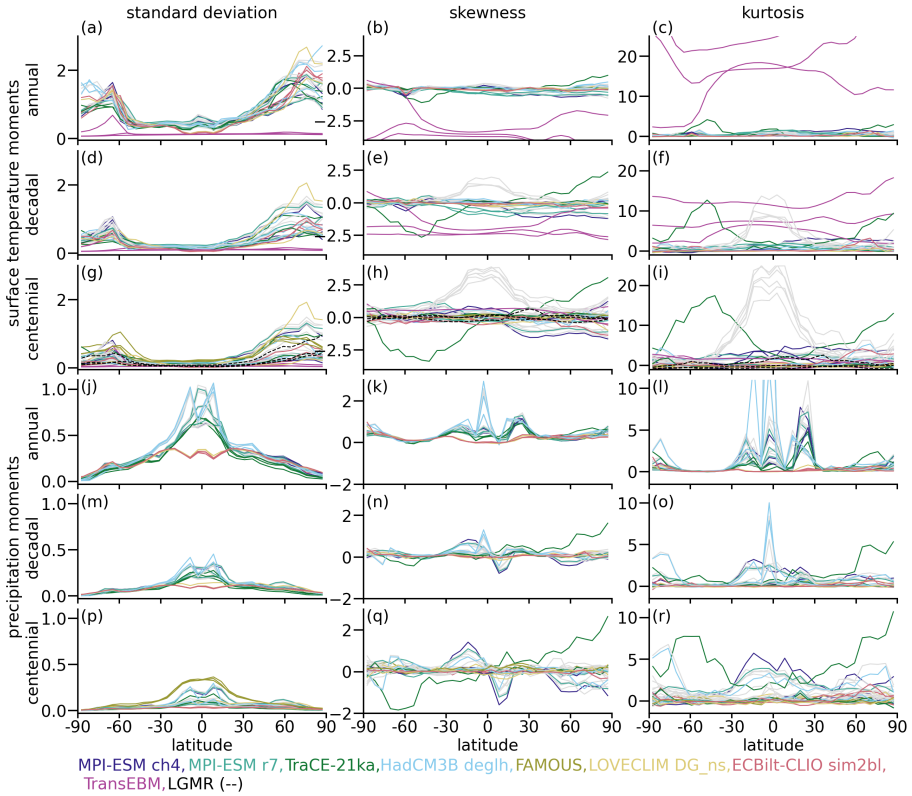

Figure S8. Changes of annual, decadal and centennial higher order moments of surface temperature (a-i) and precipitation (j-r) with latitude as in Fig. 5, but for the individual simulations of the main set. Here, standard deviation (left column), skewness (middle column) and kurtosis (right column) are shown. For each simulation LGM, Deglaciation and Holocene are shown. The sensitivity set of simulations are shown in gray.

Schiemann, R., Demory, M.-E., Mizielinski, M. S., Roberts, M. J., Shaffrey, L. C., Strachan, J., and Vidale, P. L.: The Sensitivity of the Tropical Circulation and Maritime Continent Precipitation to Climate Model Resolution, Climate Dynamics, 42, 2455–2468, https://doi.org/10.1007/s00382-013-1997-0, 2014.

Schindlbeck-Belo, J. C., Toohey, M., Jegen, M., Kutterolf, S., and Rehfeld, K.: PalVol v1: A Proxy-Based Semi-Stochastic Ensemble Reconstruction of Volcanic Stratospheric Sulfur Injection for the Last Glacial Cycle (130,000–50 BP), Earth System Science Data Discussions, pp. 1–32, https://doi.org/10.5194/essd-2023-103, 2023.

Steinhilber, F., Beer, J., and Fröhlich, C.: Total Solar Irradiance during the Holocene, Geophysical Research Letters, 36, 1–5, https://doi.org/10.1029/2009GL040142, 2009.

Theiler, J., Eubank, S., Longtin, A., Galdrikian, B., and Doyne Farmer, J.: Testing for Nonlinearity in Time Series: The Method of Surrogate Data, Physica D: Nonlinear Phenomena, 58, 77–94, https://doi.org/10.1016/0167-2789(92)90102-S, 1992.

Zhuang, K., North, G. R., and Stevens, M. J.: A NetCDF Version of the Two-Dimensional Energy Balance Model Based on the Full Multigrid Algorithm, SoftwareX, 6, 198–202, https://doi.org/10.1016/j.softx.2017.07.003, 2017.

Ziegler, E. and Rehfeld, K.: TransEBM v. 1.0: Description, Tuning, and Validation of a Transient Model of the Earth's Energy Balance in Two Dimensions, Geoscientific Model Development, 14, 2843–2866, https://doi.org/10.5194/gmd-14-2843-2021, 2021.

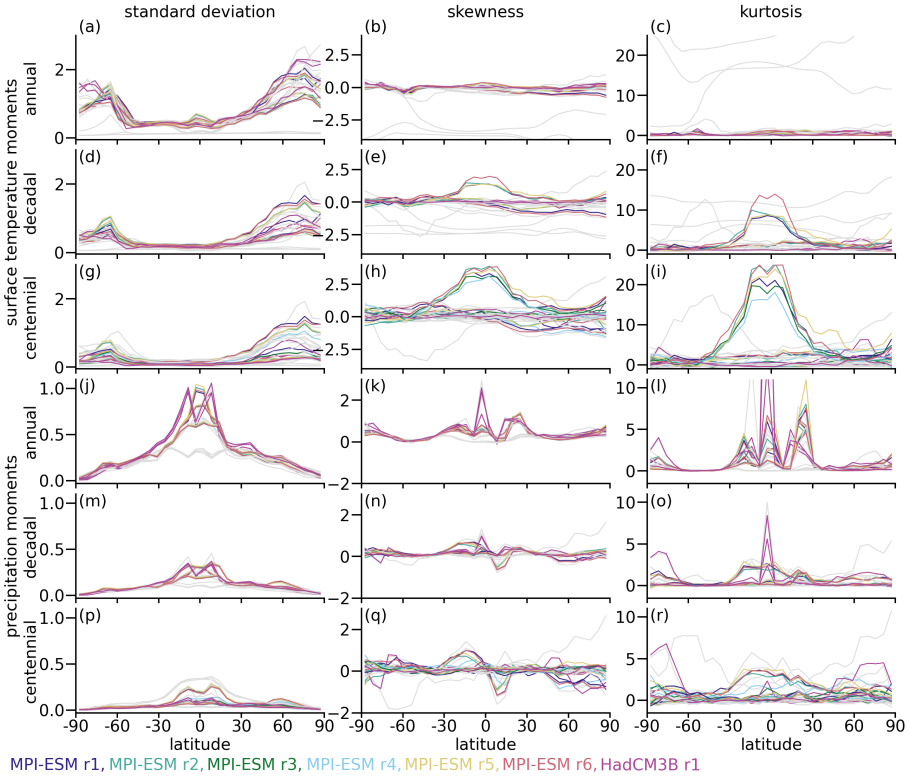

Figure S9. Same as in Fig. S9, but for the sensitivity set.

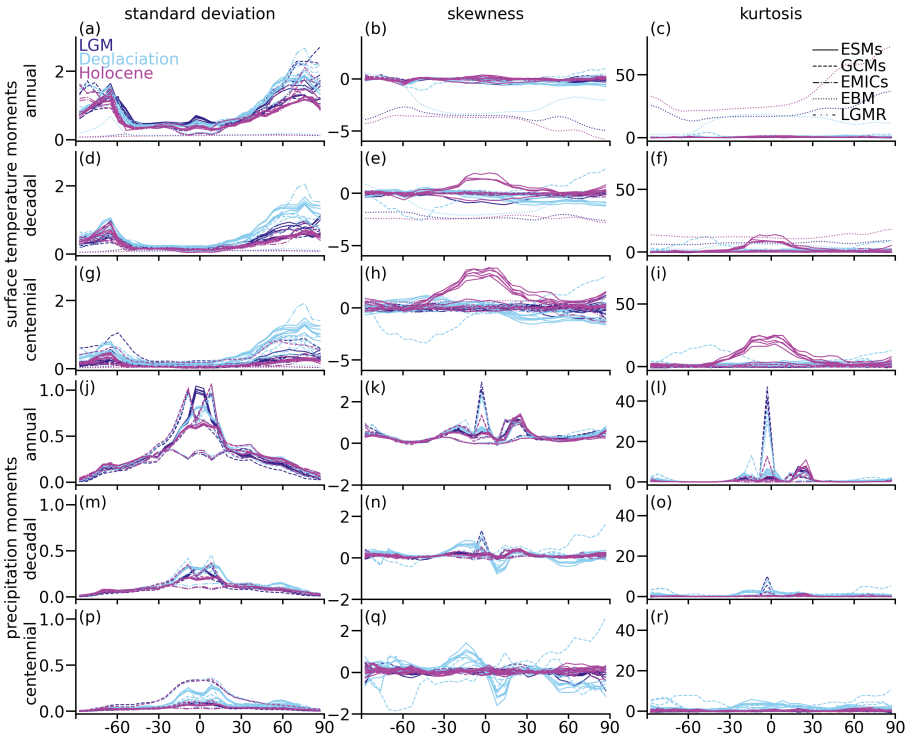

Figure S10. Changes of annual, decadal and centennial higher order moments of surface temperature (a-i) and precipitation (j-r) with latitude as in Fig. 5 but shown highlighting the changes between LGM, Deglaciation and Holocene.

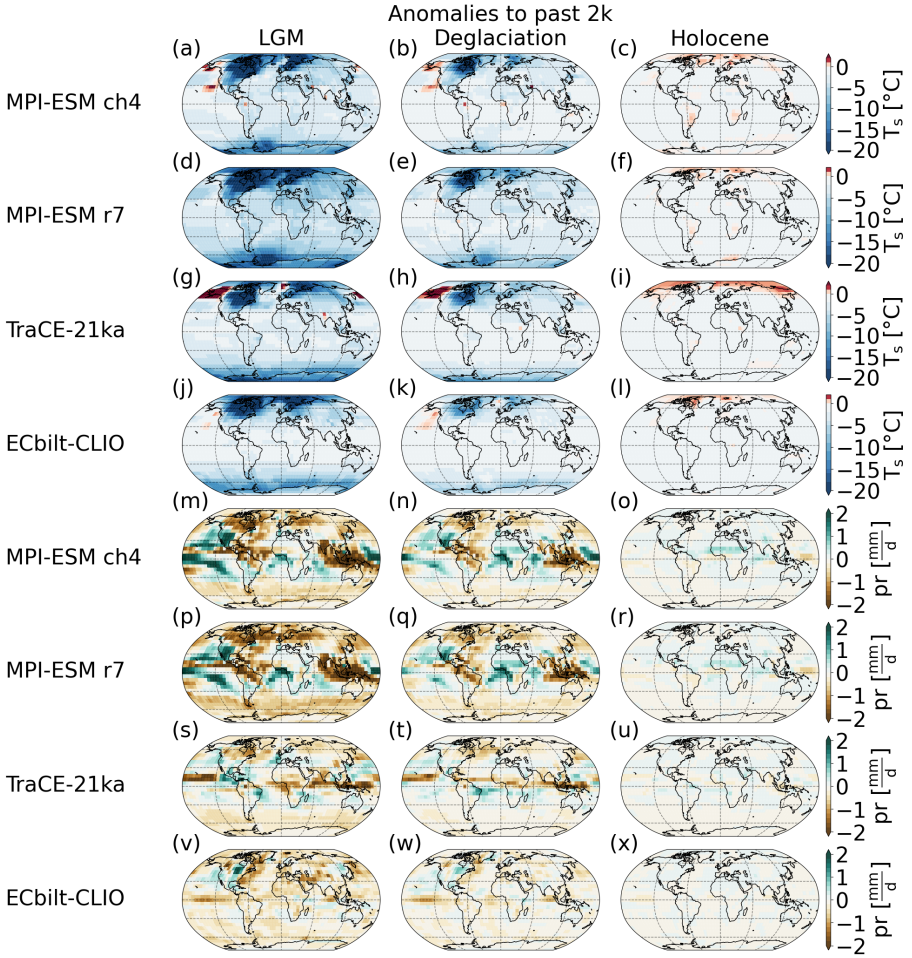

Figure S11. Exemplary mean anomalies of surface temperature (a – l) and precipitation (m – x) for the LGM (left column), Deglaciation (middle column) and Holocene (right column). For each of these, MPI-ESM ch4, MPI-ESM r7, TraCE-21ka and ECBilt-CLIO are shown.

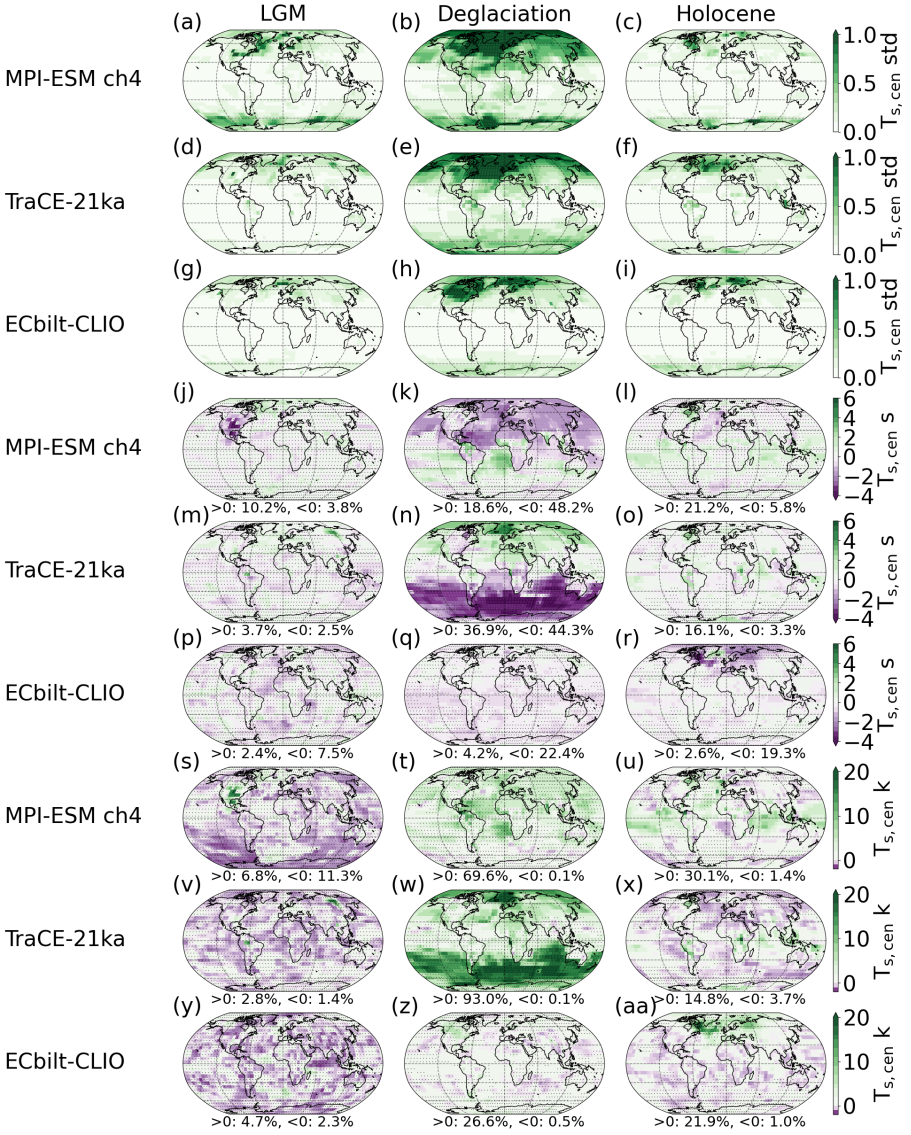

Figure S12. Exemplary patterns of change in centennial standard deviation (a – i), skewness (j – r) and kurtosis (s – aa) of surface temperature for the LGM (left column), Deglaciation (middle column) and Holocene (right column). For each of these, MPI-ESM ch4, TraCE-21ka and ECBilt-CLIO are shown. For skewness and kurtosis, the percentages of grid boxes with significant positive and negative deviations from a Gaussian distribution are given and non-significant changes are hatched.

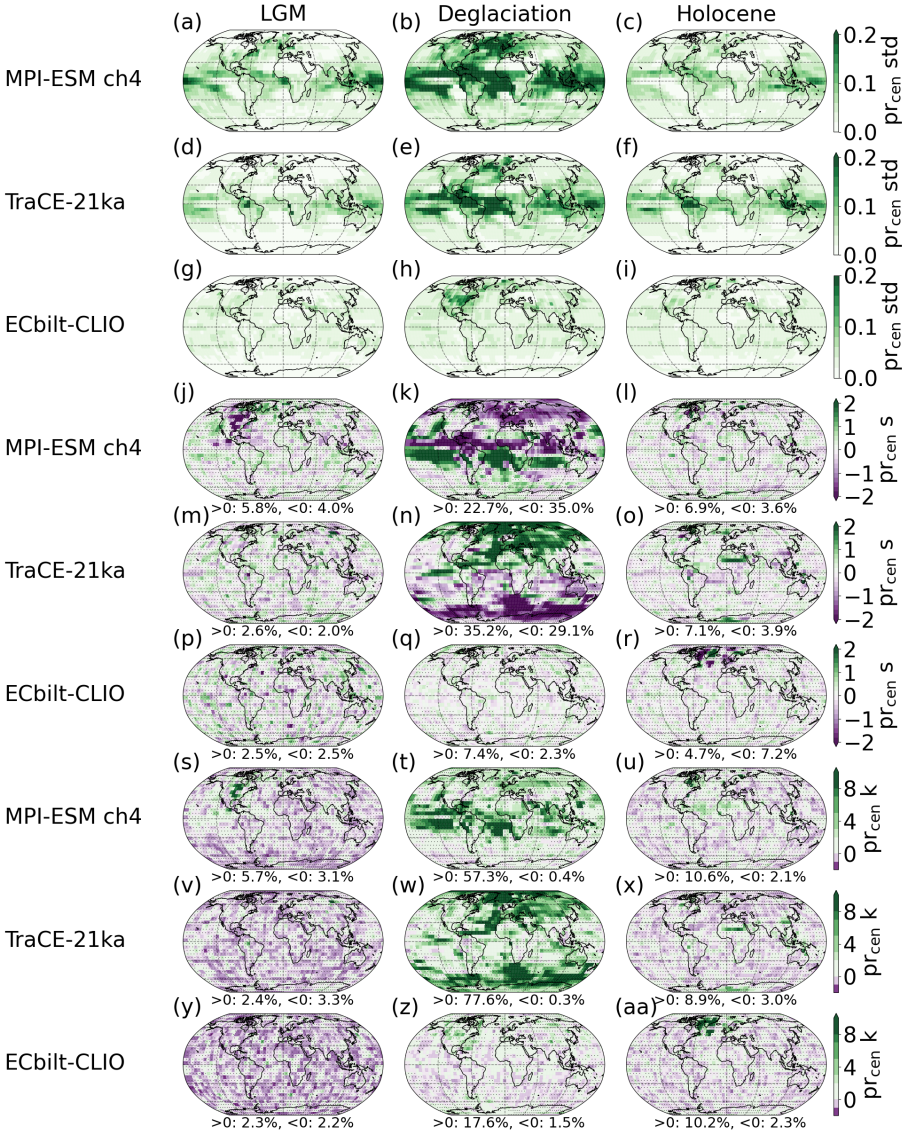

Figure S13. Exemplary patterns of change in centennial standard deviation (a – i), skewness (j – r) and kurtosis (s – aa) of precipitation for the LGM (left column), Deglaciation (middle column) and Holocene (right column). For each of these, MPI-ESM ch4, TraCE-21ka and ECBilt-CLIO are shown. For skewness and kurtosis, the percentages of grid boxes with significant positive and negative deviations from a Gaussian distribution are given and non-significant changes are hatched.

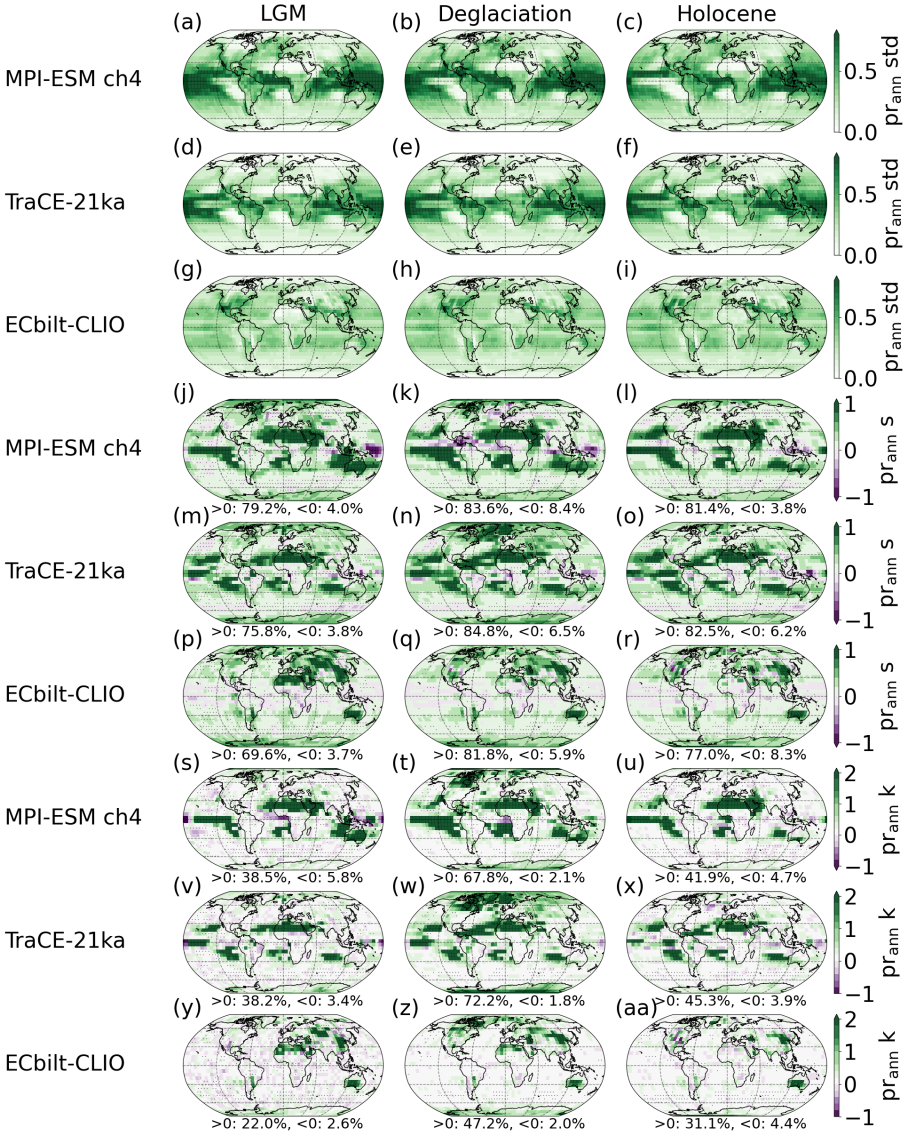

Figure S14. Exemplary patterns of change in annual standard deviation (a – i), skewness (j – r) and kurtosis (s – aa) of precipitation for the LGM (left column), Deglaciation (middle column) and Holocene (right column). For each of these, MPI-ESM ch4, TraCE-21ka and ECBilt-CLIO are shown. For skewness and kurtosis, the percentages of grid boxes with significant positive and negative deviations from a Gaussian distribution are listed and non-significant changes are hatched.

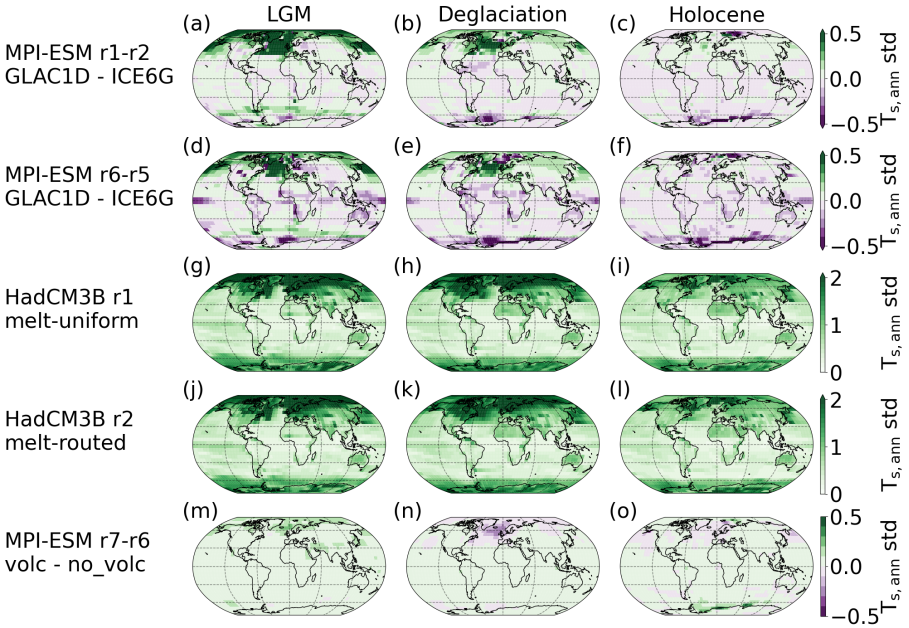

Figure S15. Regional effects of forcings on annual standard deviation of surface temperature. Forcings are noted along with the run name for each row.

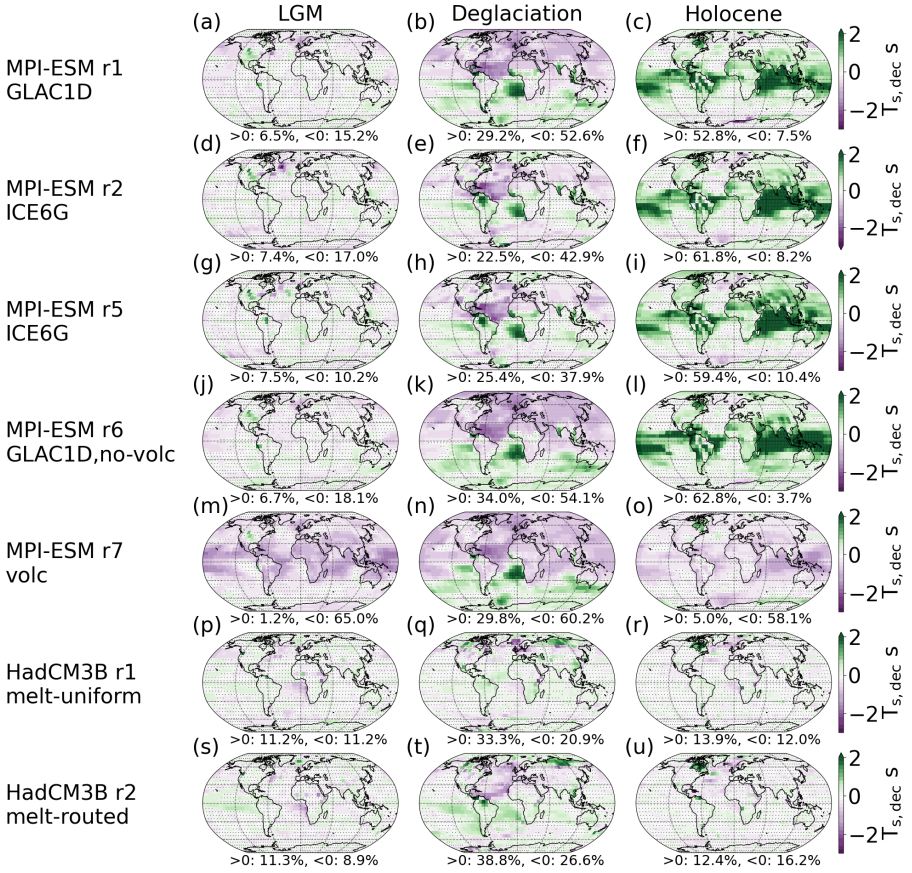

Figure S16. Regional effects of forcings on decadal skewness of surface temperature. Forcings are noted along with the run name for each row. Percentages of grid boxes with significant positive and negative deviations from a Gaussian distribution are listed. Areas, where changes are non-significant, are hatched.

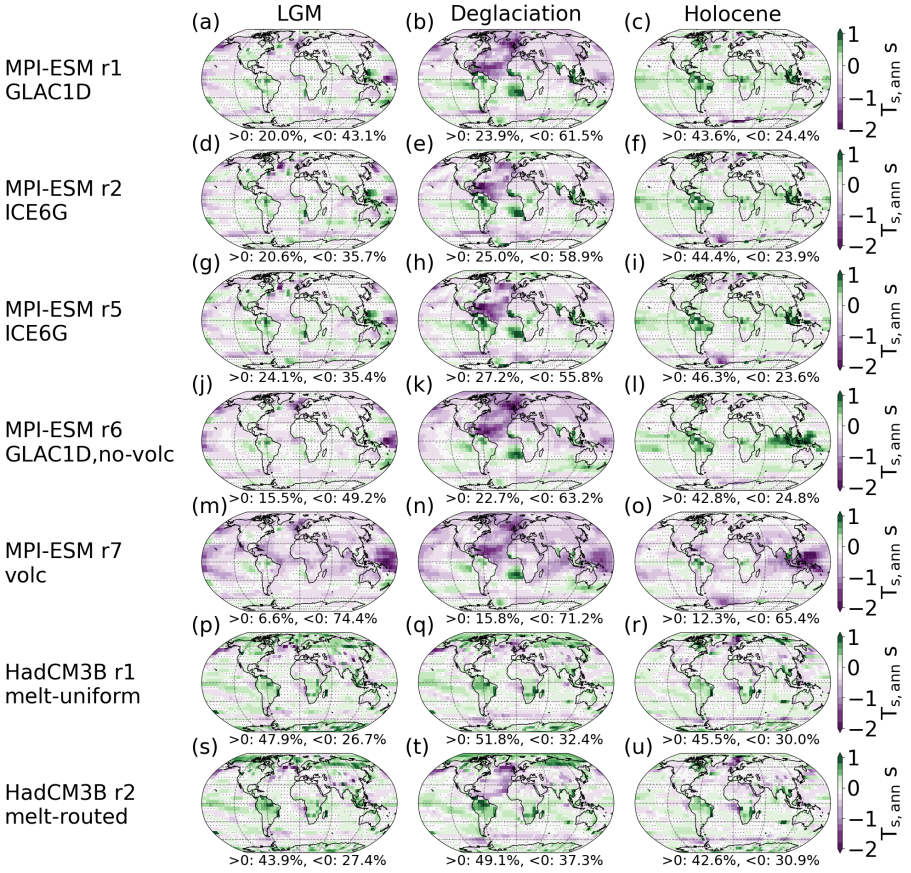

Figure S17. Regional effects of forcings on annual skewness of surface temperature. Forcings are noted along with the run name for each row. Percentages of grid boxes with significant positive and negative deviations from a Gaussian distribution are listed. Areas, where changes are non-significant, are hatched.

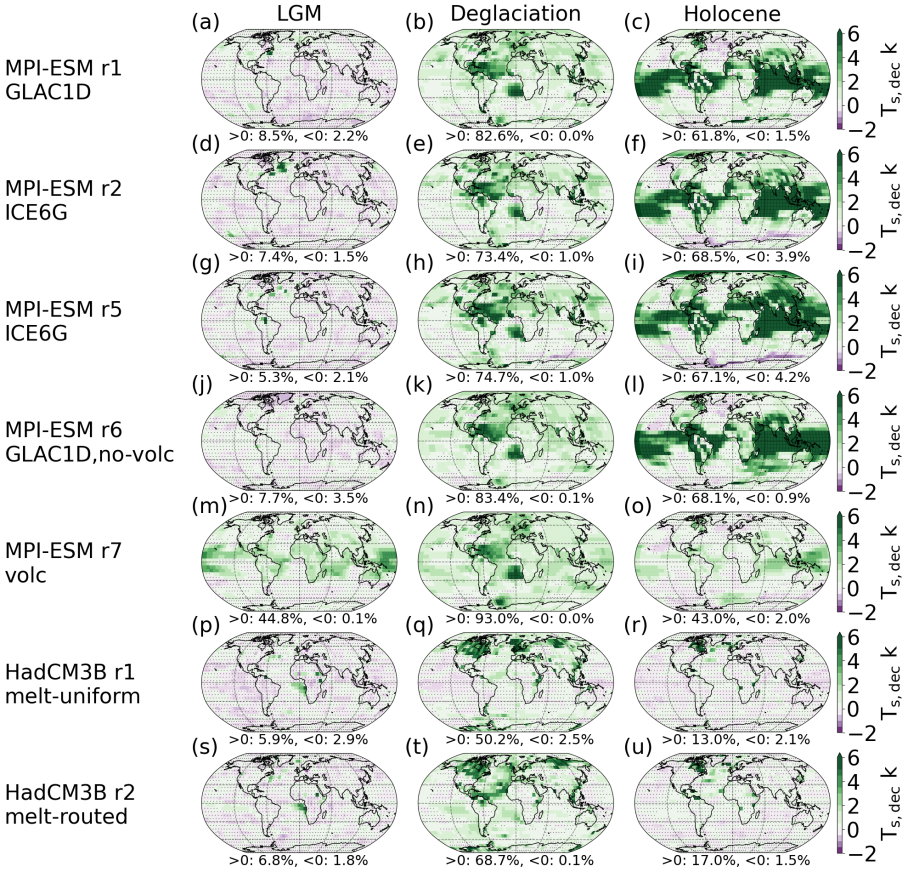

Figure S18. Regional effects of forcings on decadal kurtosis of surface temperature. Forcings are noted along with the run name for each row. Percentages of grid boxes with significant positive and negative deviations from a Gaussian distribution are listed. Areas, where changes are non-significant, are hatched.

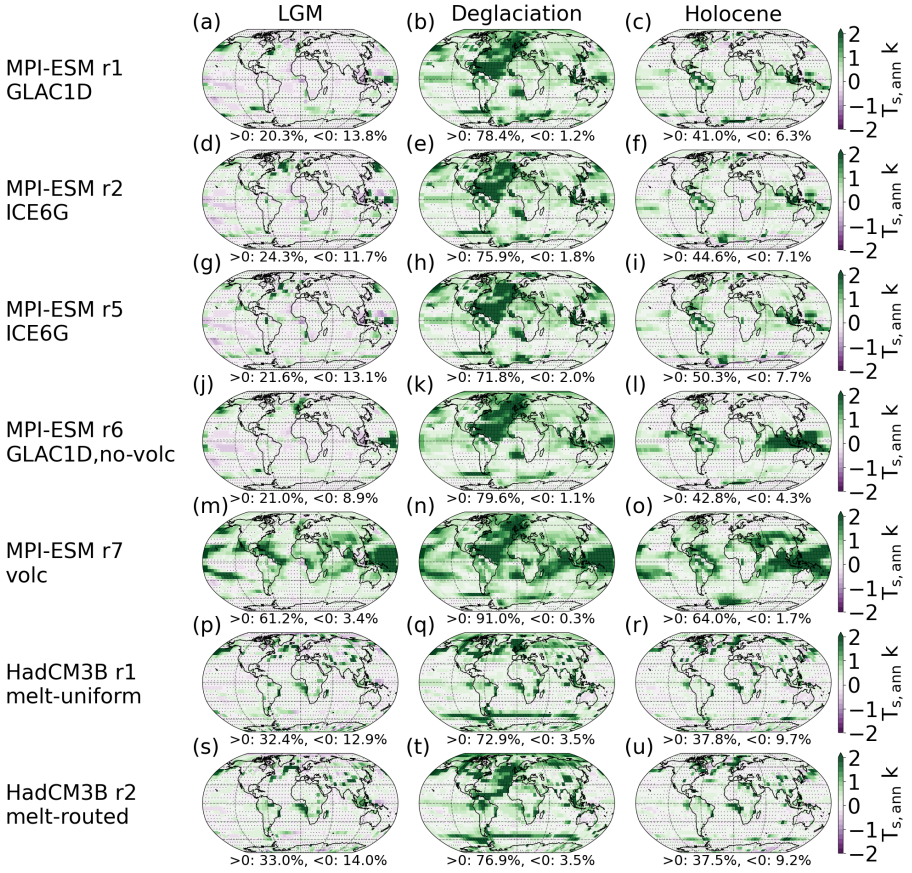

Figure S19. Regional effects of forcings on annual kurtosis of surface temperature. Forcings are noted along with the run name for each row. Percentages of grid boxes with significant positive and negative deviations from a Gaussian distribution are listed. Areas, where changes are non-significant, are hatched.

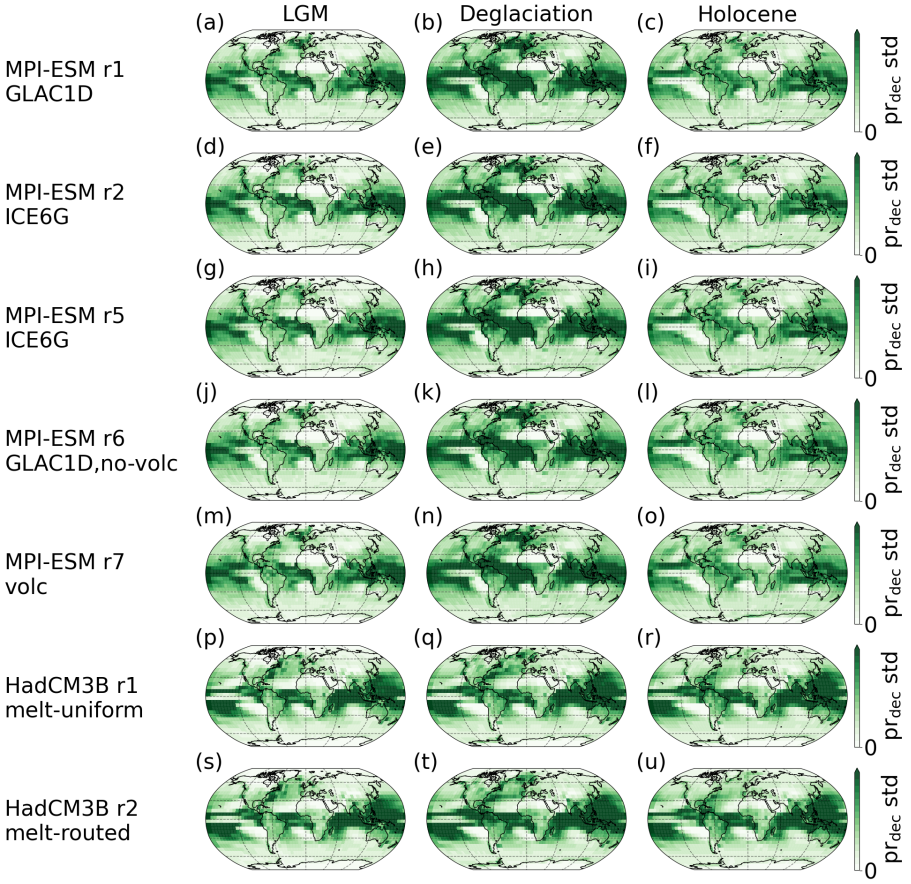

Figure S20. Regional effects of forcings on decadal standard deviation of precipitation. Forcings are noted along with the run name for each row.

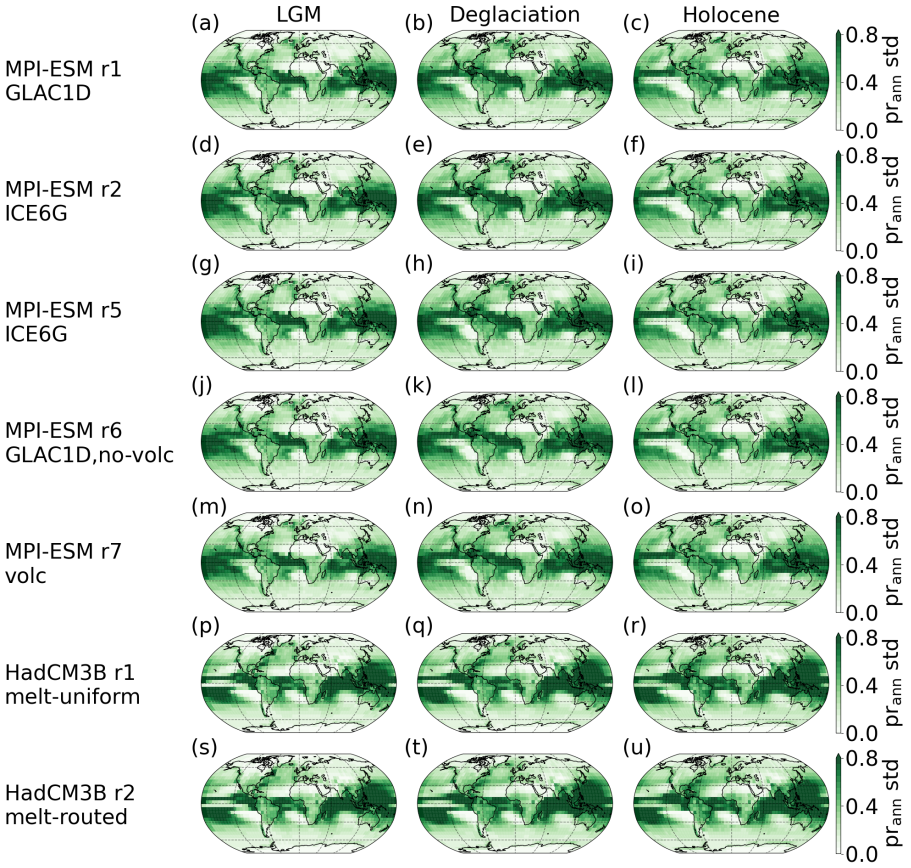

Figure S21. Regional effects of forcings on annual skewness of precipitation. Forcings are noted along with the run name for each row.

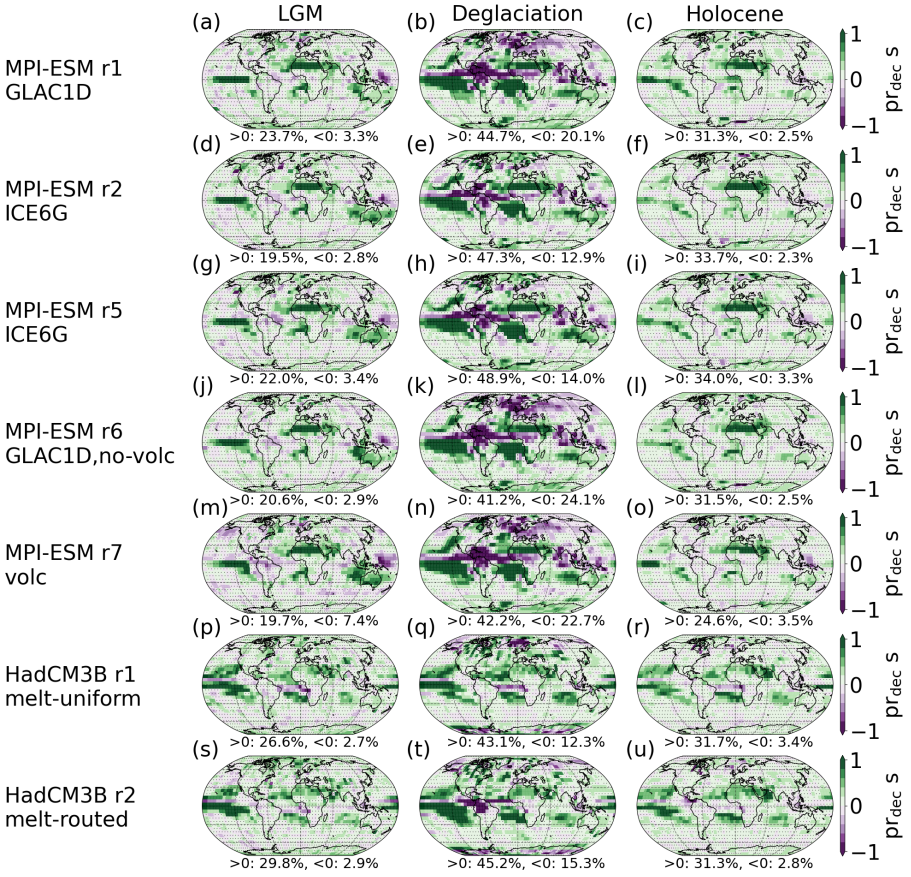

Figure S22. Regional effects of forcings on decadal skewness of precipitation. Forcings are noted along with the run name for each row. Percentages of grid boxes with significant positive and negative deviations from a Gaussian distribution are listed. Areas, where changes are non-significant, are hatched.

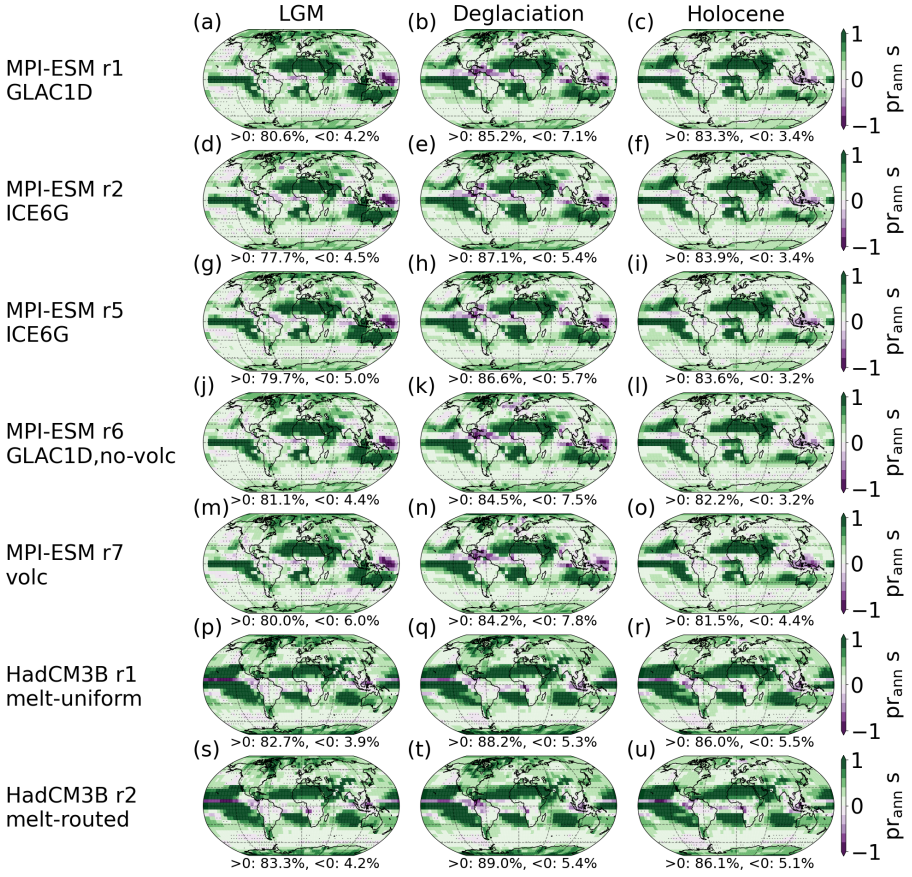

Figure S23. Regional effects of forcings on annual skewness of precipitation. Forcings are noted along with the run name for each row. Percentages of grid boxes with significant positive and negative deviations from a Gaussian distribution are listed. Areas, where changes are non-significant, are hatched.

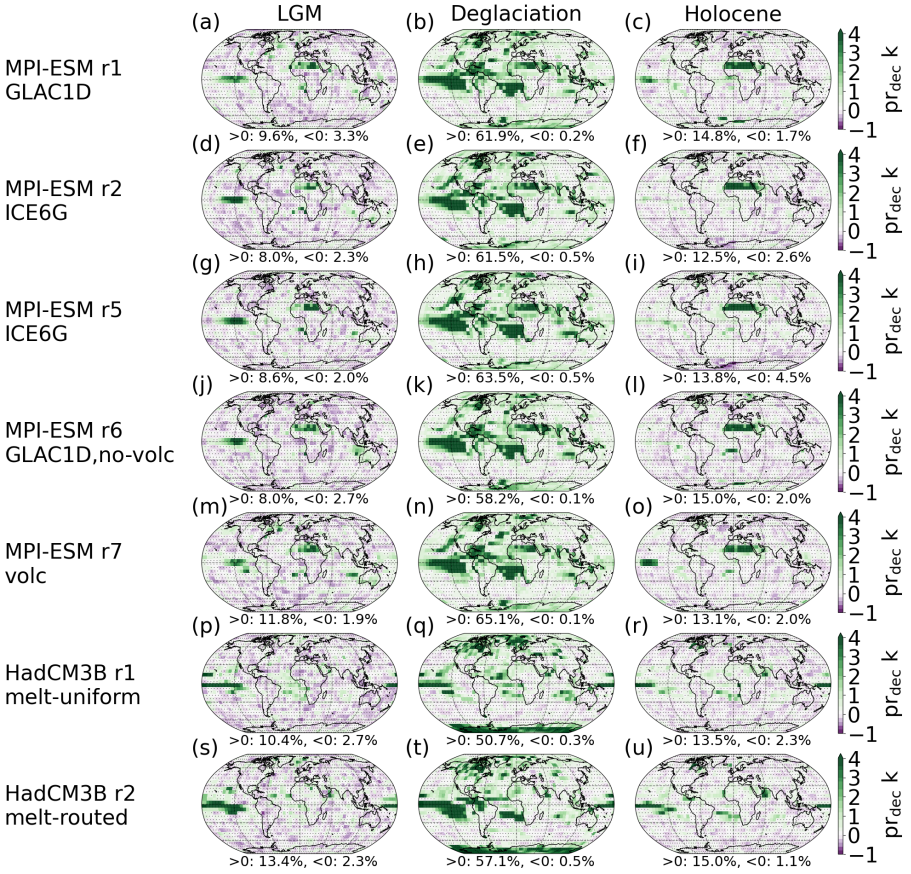

Figure S24. Regional effects of forcings on decadal kurtosis of precipitation. Forcings are noted along with the run name for each row. Percentages of grid boxes with significant positive and negative deviations from a Gaussian distribution are listed. Areas, where changes are non-significant, are hatched.

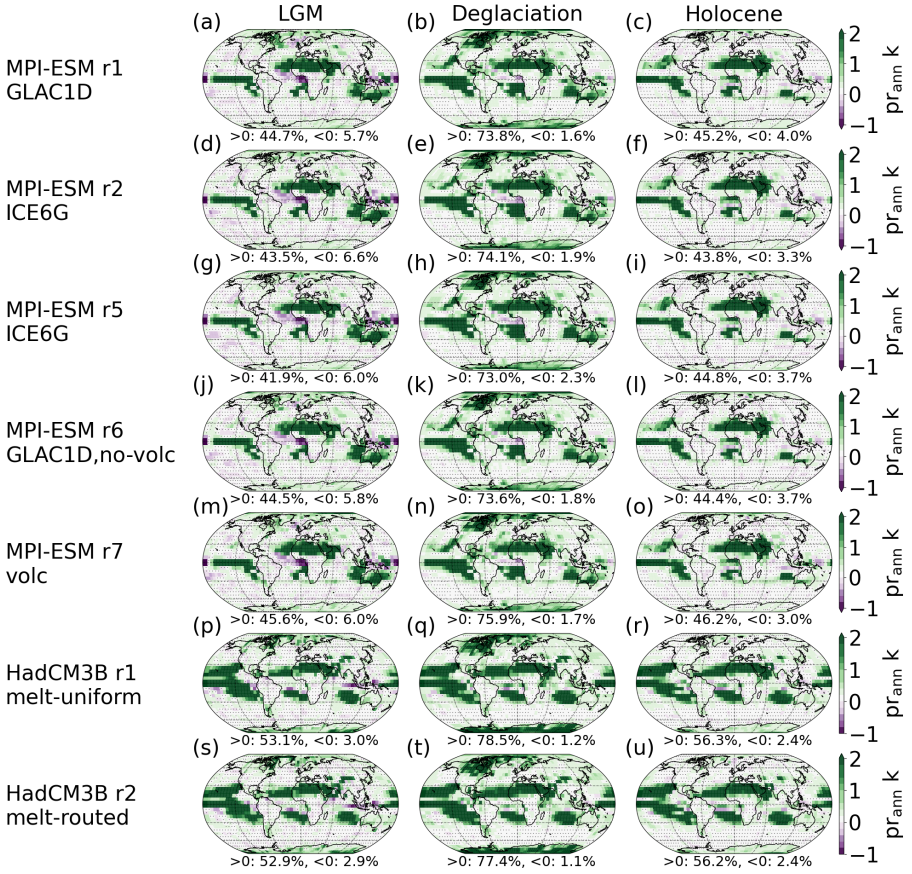

Figure S25. Regional effects of forcings on annual kurtosis of precipitation. Forcings are noted along with the run name for each row. Percentages of grid boxes with significant positive and negative deviations from a Gaussian distribution are listed. Areas, where changes are non-significant, are hatched.

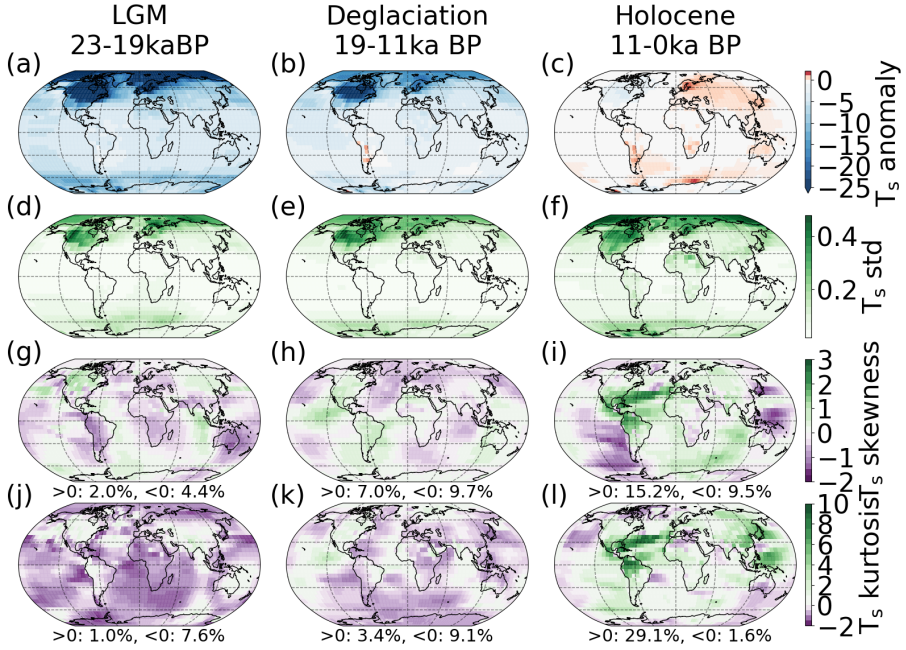

Figure S26. Spatial patterns in the surface temperature moments of LGMR for (a) – (c) mean, (d) – (f) standard deviation, (g) – (i) skewness and (j) – (l) kurtosis. For skewness and kurtosis, percentages of grid boxes with significant positive and negative deviations from a Gaussian distribution are listed and non-significant changes hatched.

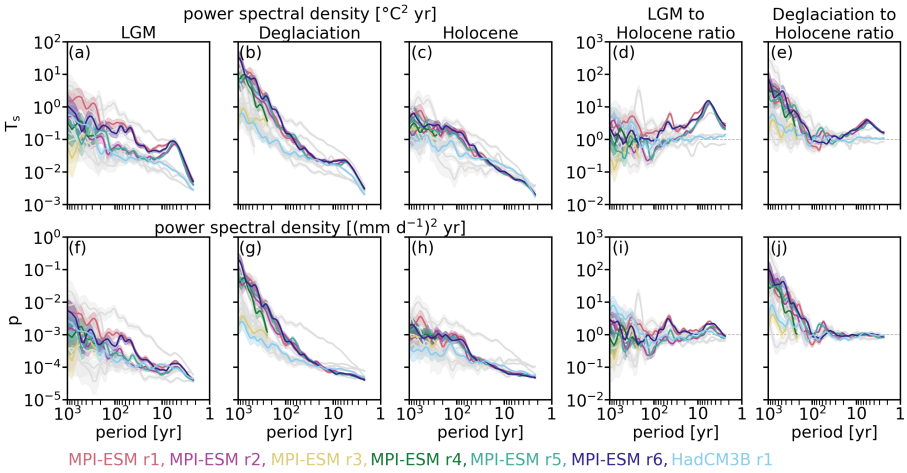

Figure S27. Spectra and spectral ratios of surface temperature (top row) and precipitation (bottom row) variability with chi-squared distributed confidence intervals. The spectra are separated by time period with (a, f) LGM, (b, g) Deglaciation and (c, h) Holocene. The spectral ratios highlight the differences between the periods showing the LGM-to-Holocene (d, i) as well the Deglaciation-to-Holocene ratio (e, j). Shown in gray are the simulations from Fig. 12.

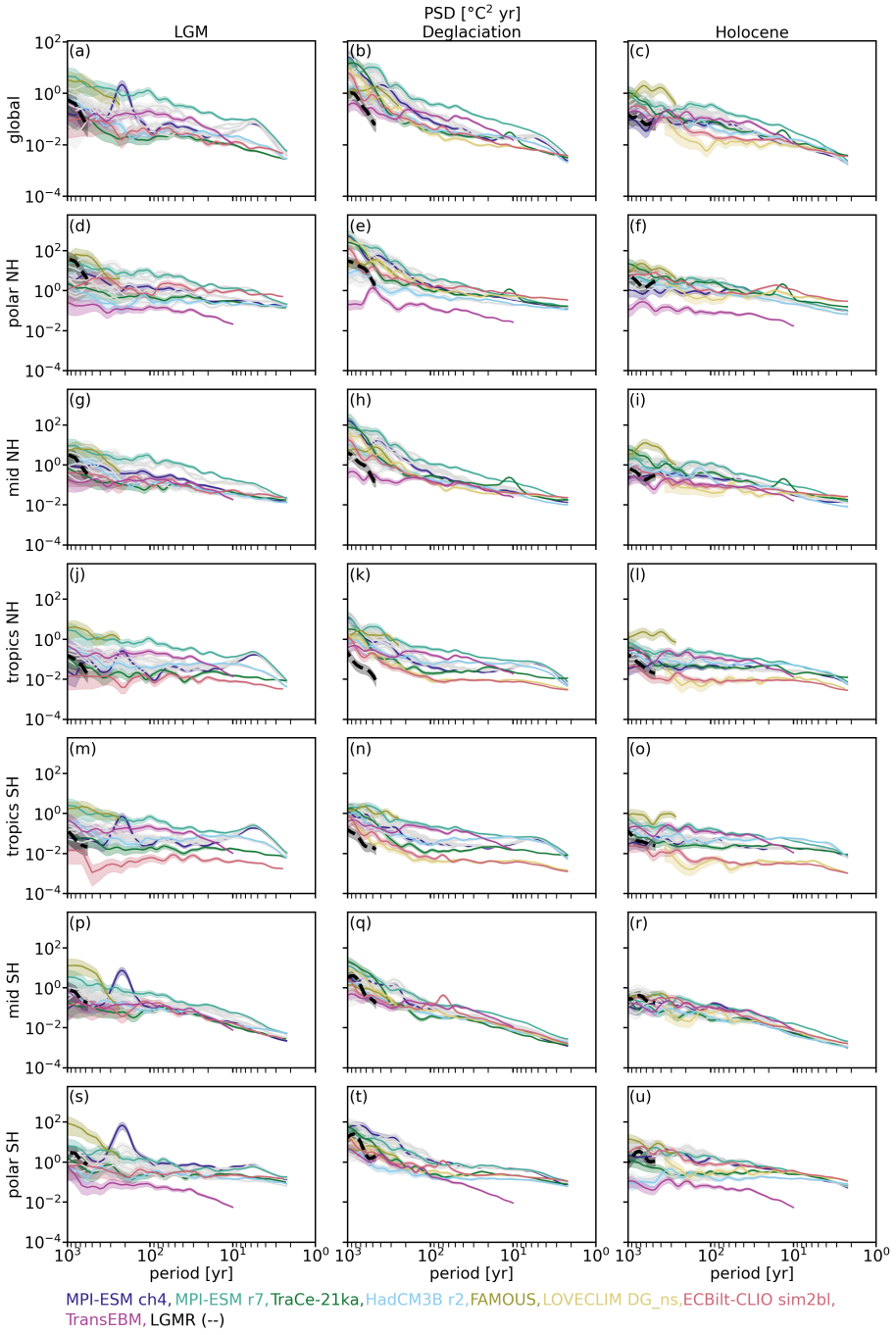

Figure S28. Global (a – c) and regional (d – u) surface temperature spectra for LGM (left column), Deglaciation (middle column) and Holocene (right column) with chi-squared distributed confidence intervals for the main set simulations. The regional spectra correspond to average timeseries of 30 degree wide latitude bands: northern polar region (60–90°N, d–f), northern mid-latitudes (30–60°N, g–i), northern tropics (0–30°N, j–l), southern tropics (0–30°S, m–o), southern mid-latitudes (30–60°S, p–r) and southern polar region (60–90°S, s–u).

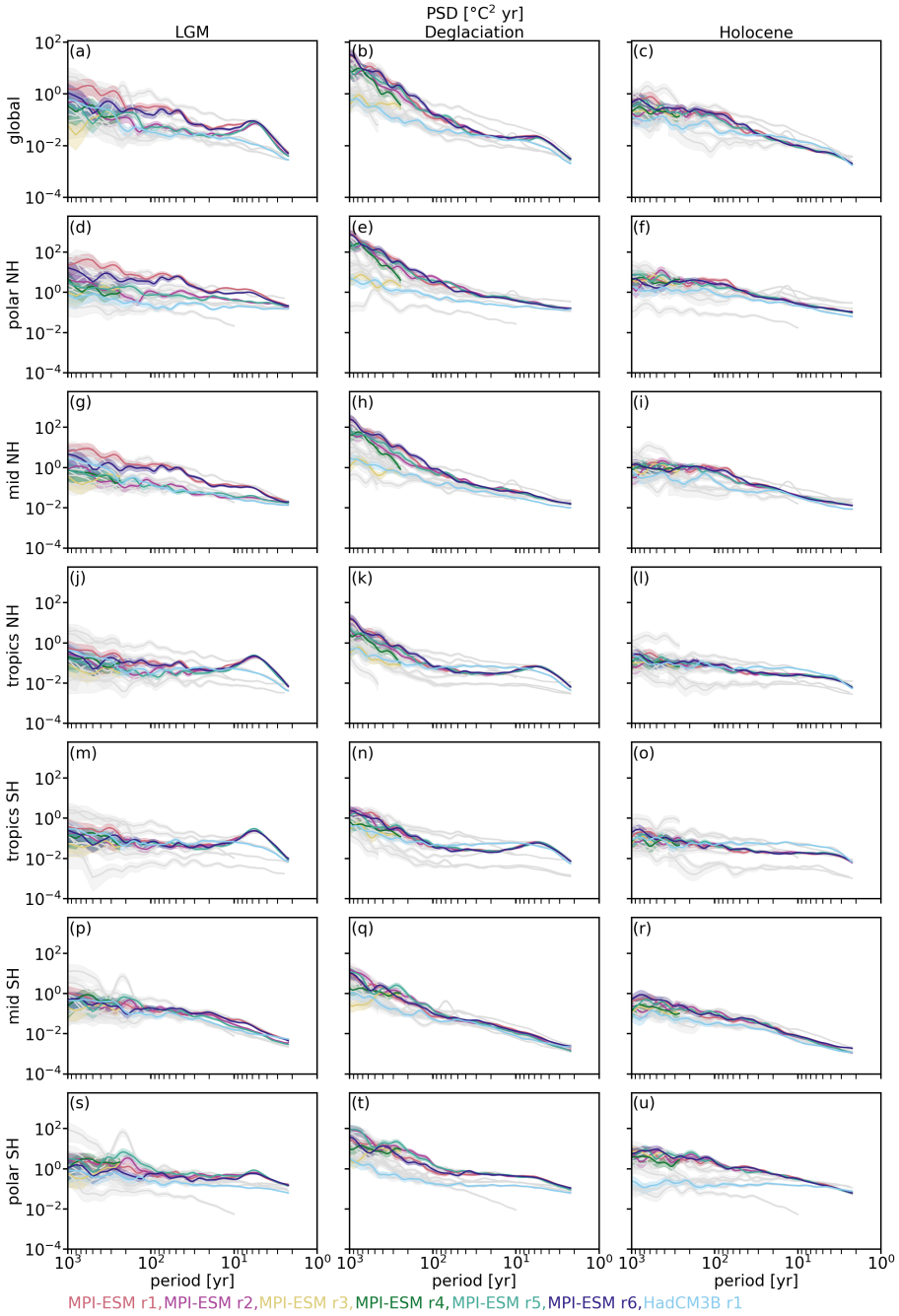

Figure S29. Same as Fig. S28 but for the sensitivity set.

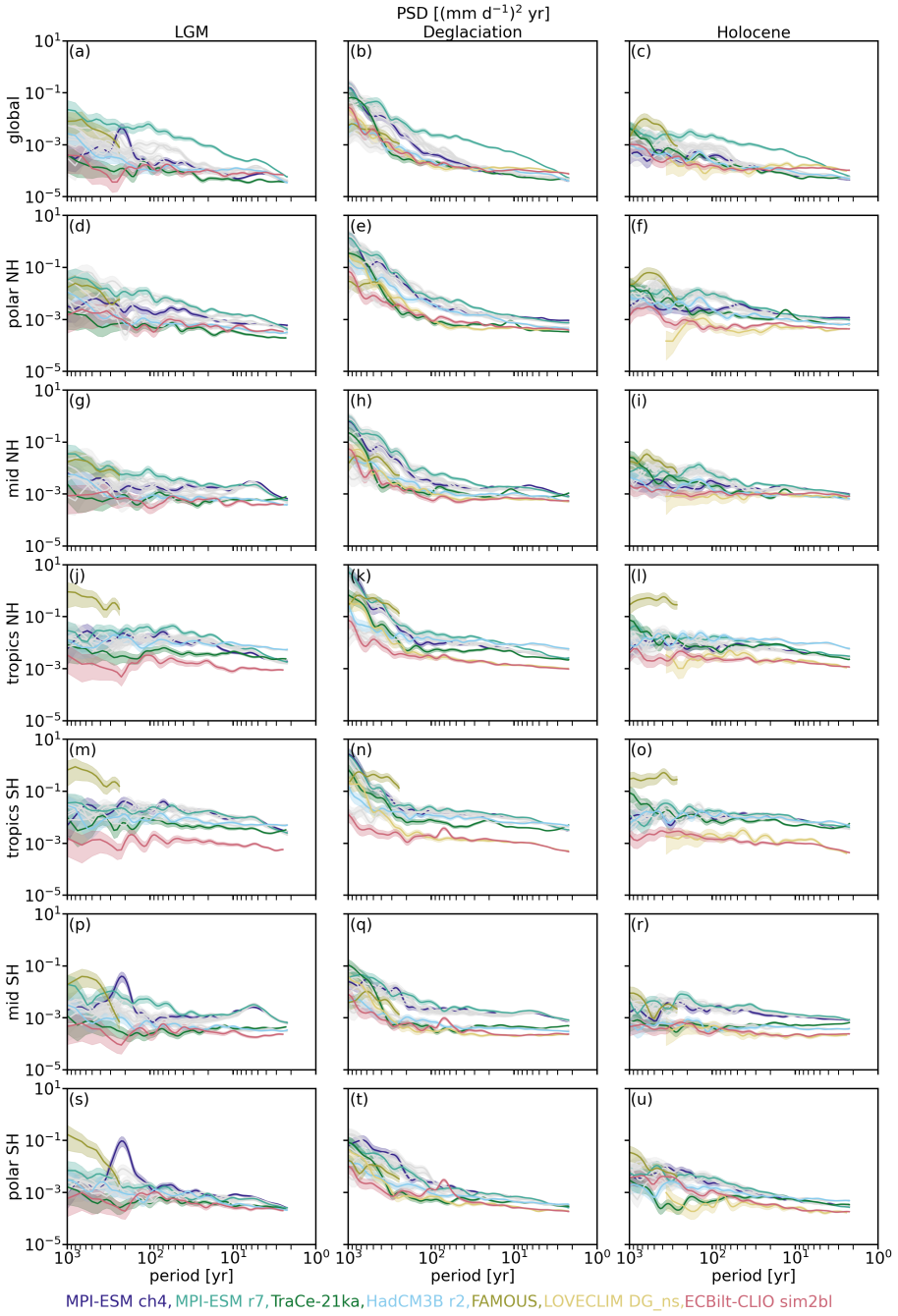

Figure S30. Same as Fig. S28 but for precipitation.

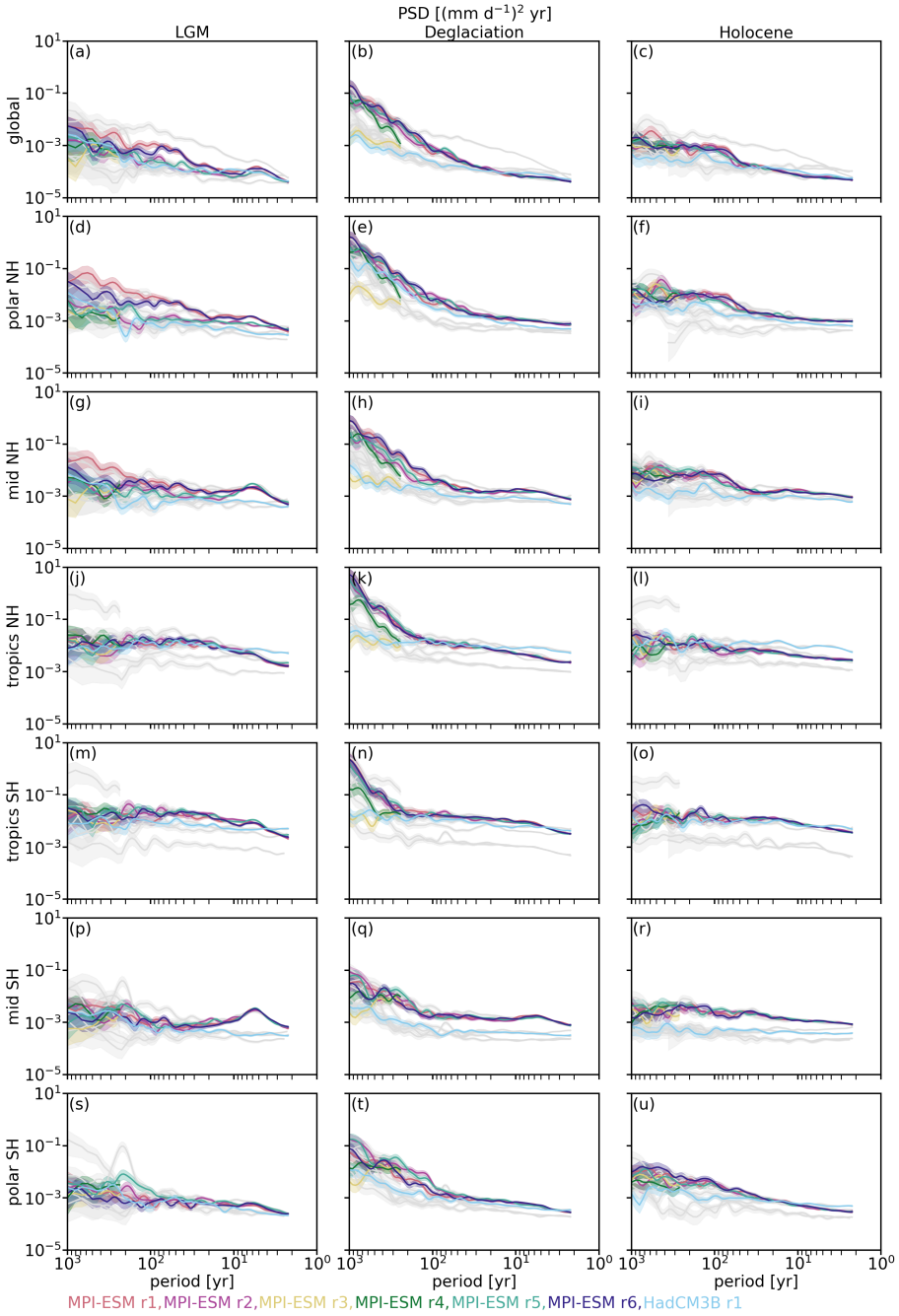

Figure S31. Same as Fig. S30 but for the sensitivity set.

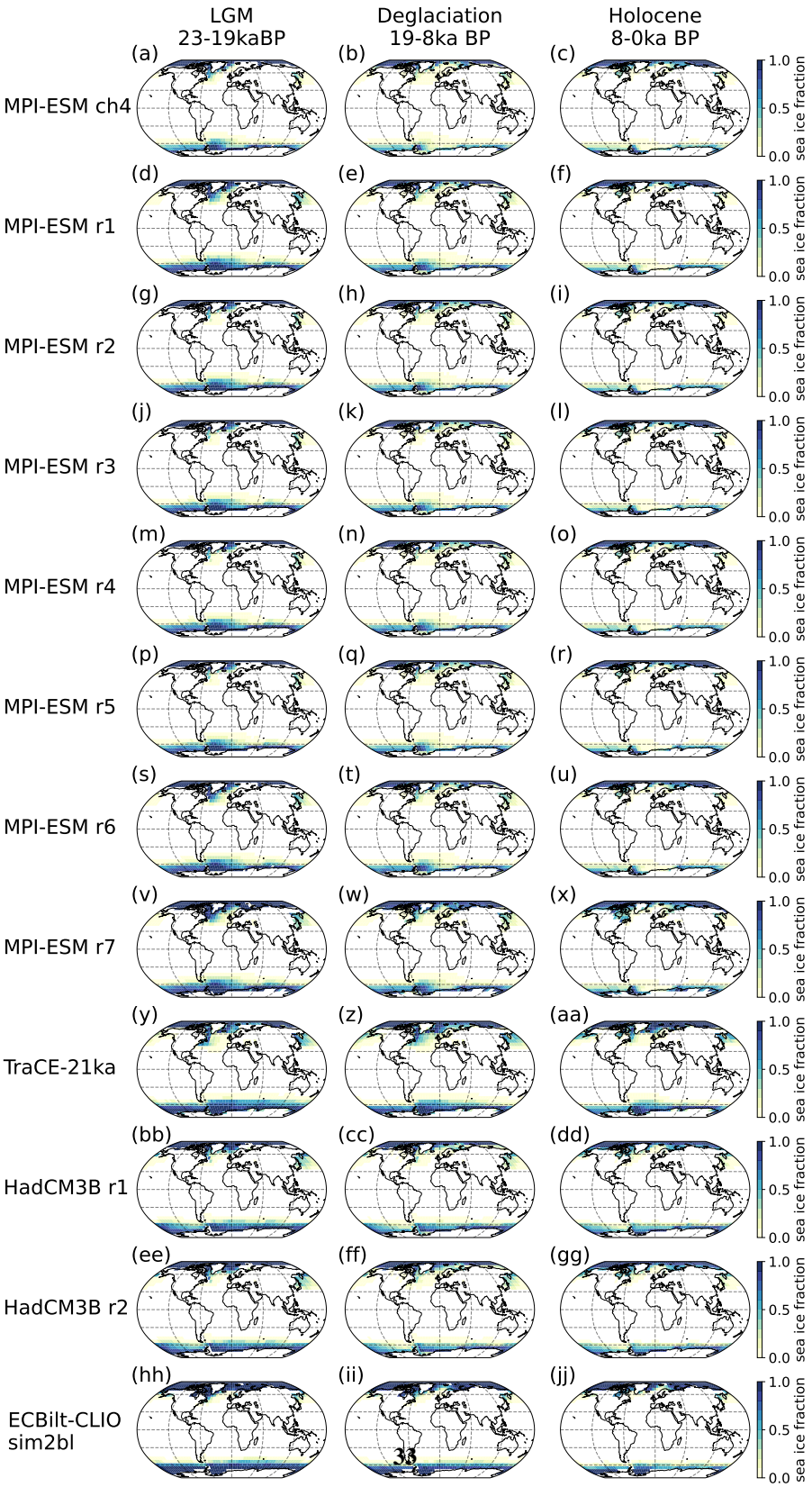

Figure S32. Global mean sea ice fraction from LGM to Holocene for simulations from the main and sensitivity set.

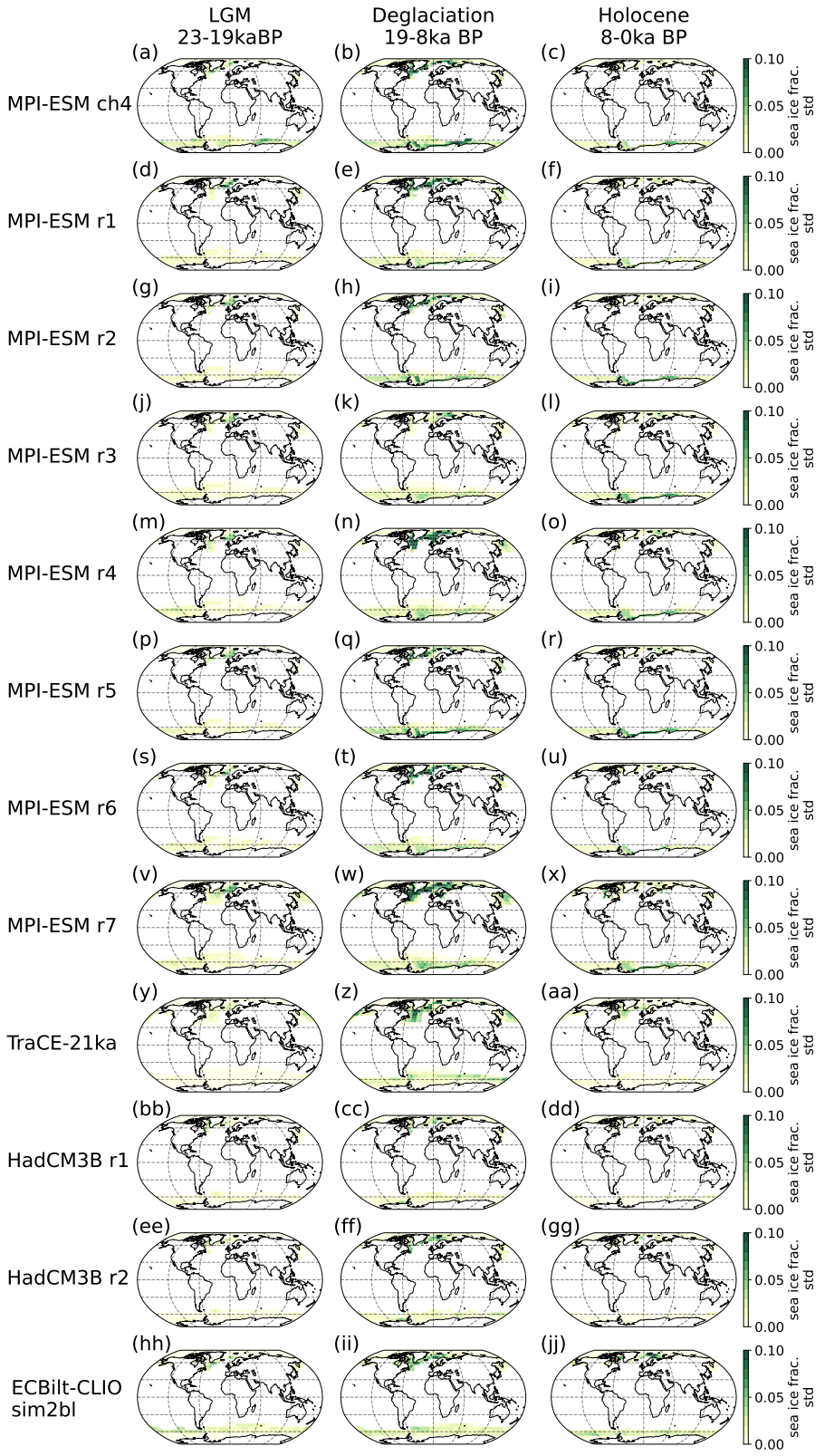

Figure S33. Global standard deviation of sea ice fraction from LGM to Holocene for simulations from the main and sensitivity set.

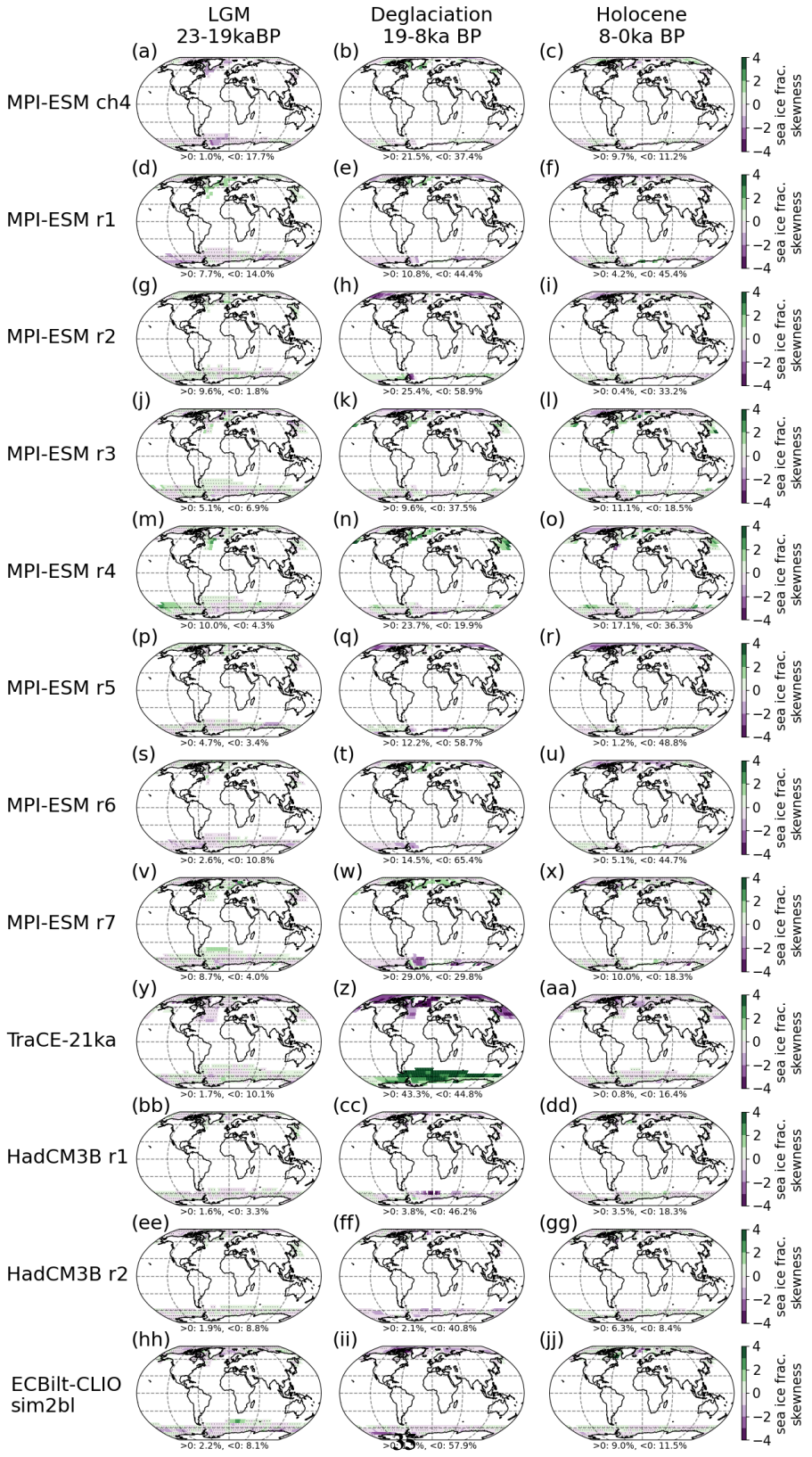

Figure S34. Global skewness of sea ice fraction from LGM to Holocene. Only areas where sea ice is constantly present were included. Percentages of grid boxes with significant positive and negative deviations from a Gaussian distribution are listed.

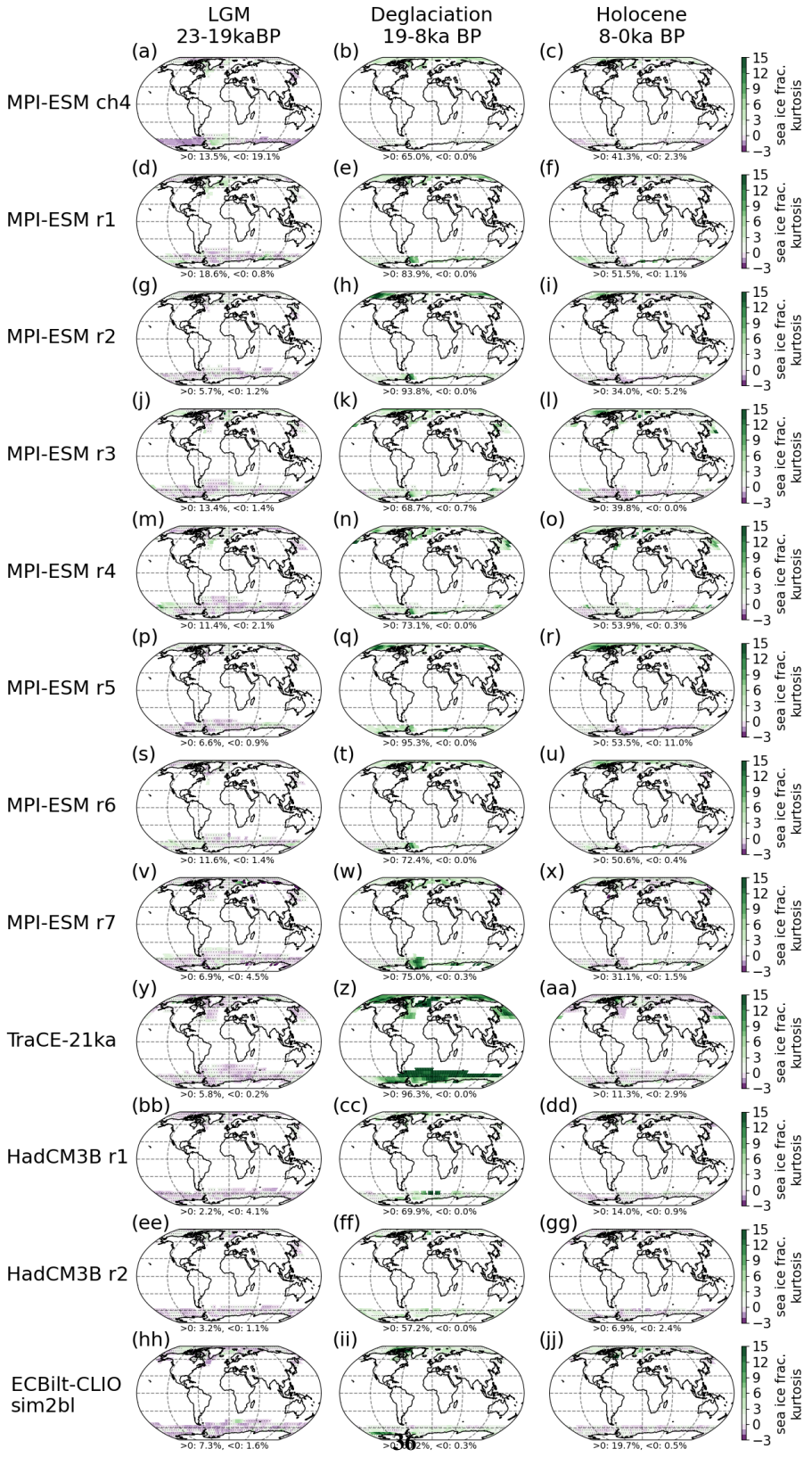

Figure S35. Global kurtosis of sea ice fraction from LGM to Holocene. Only areas where sea ice is constantly present were included. Percentages of grid boxes with significant positive and negative deviations from a Gaussian distribution are listed.

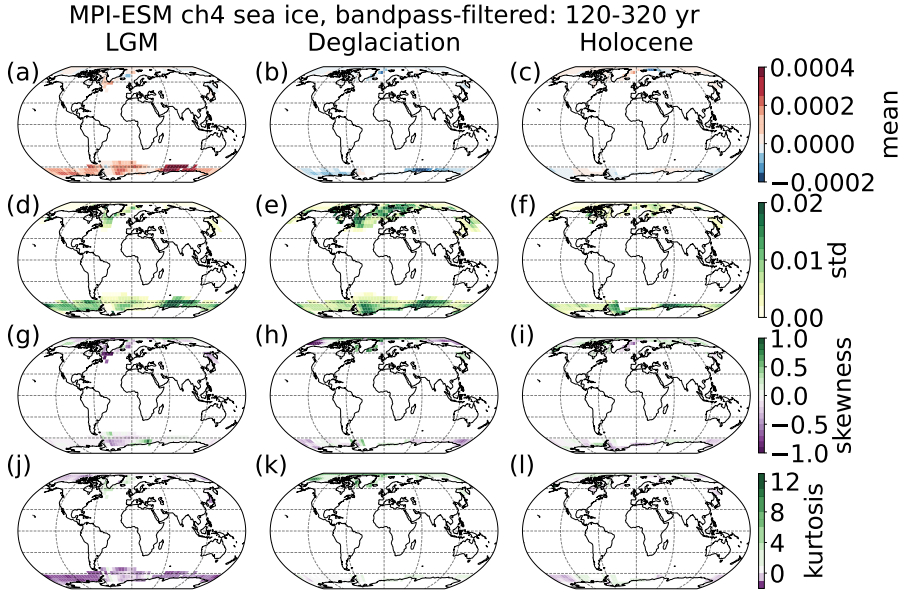

Figure S36. Bandpass-filtered (120–320 yr) moments of MPI-ESM ch4 sea ice from top row to bottom row mean, standard deviation, skewness and kurtosis for LGM (left), Deglaciation (middle) and Holocene (right). Percentages of grid boxes with significant positive and negative deviations from a Gaussian distribution are listed for skewness and kurtosis. Note that areas where sea ice disappears on centennial scale during a period were excluded during the investigation of skewness and kurtosis.

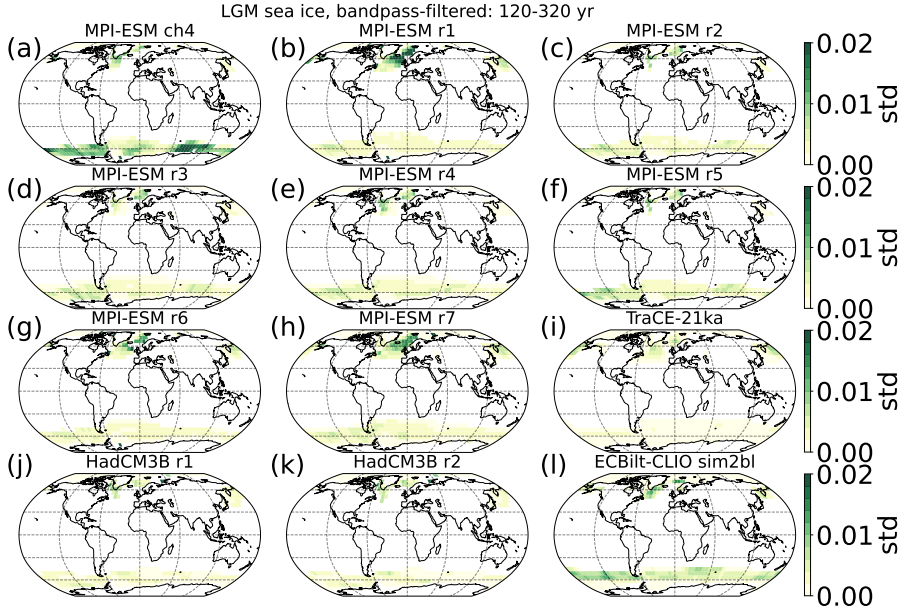

Figure S37. Bandpass-filtered (120–320 yr) standard deviation for simulations from the main and sensitivity set.

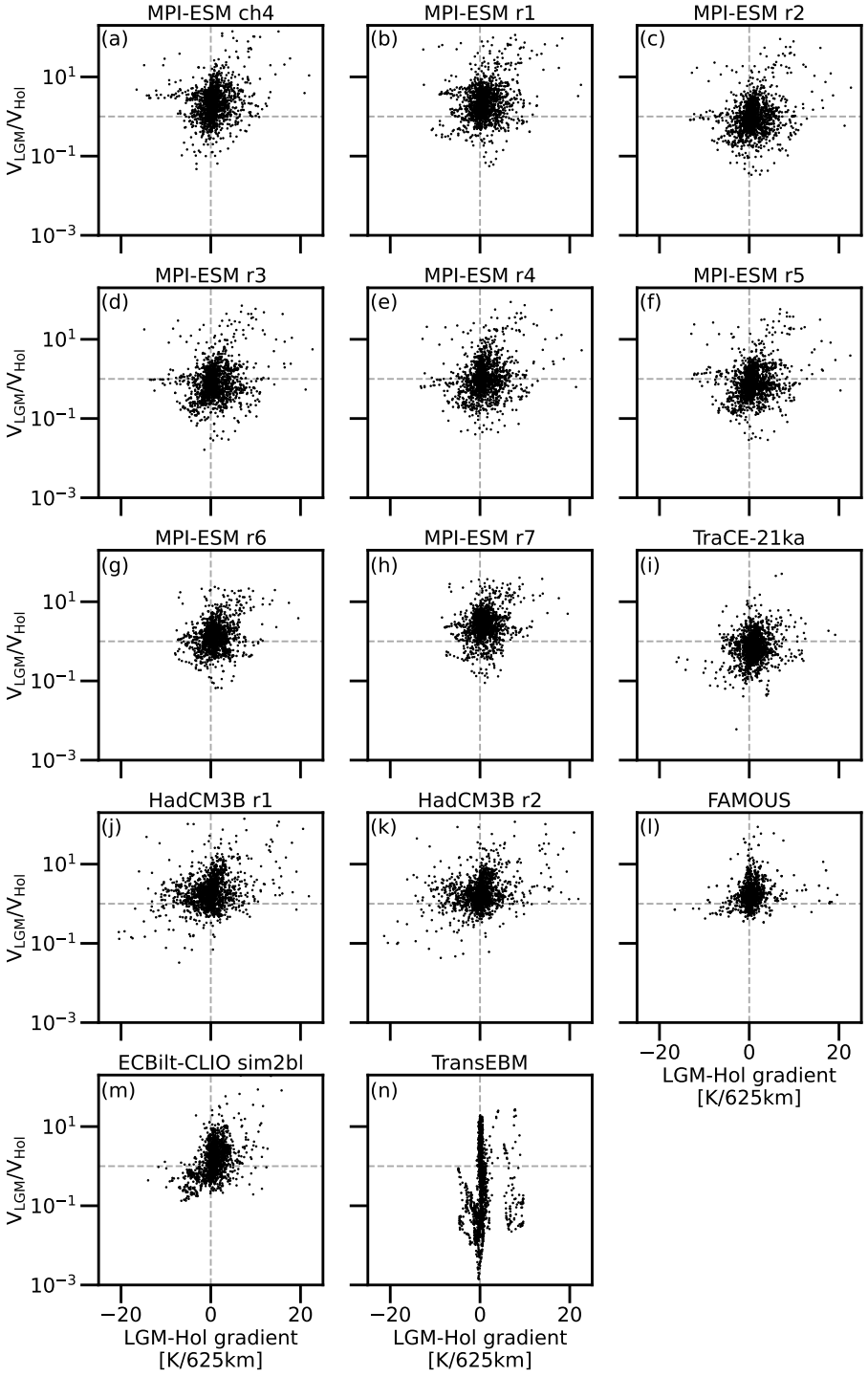

Figure S38. Global LGM-to-Holocene variance ratio against the change in meridional temperature gradient. A variance ratio of 1 and no change in meridional temperature gradient are marked by gray lines.

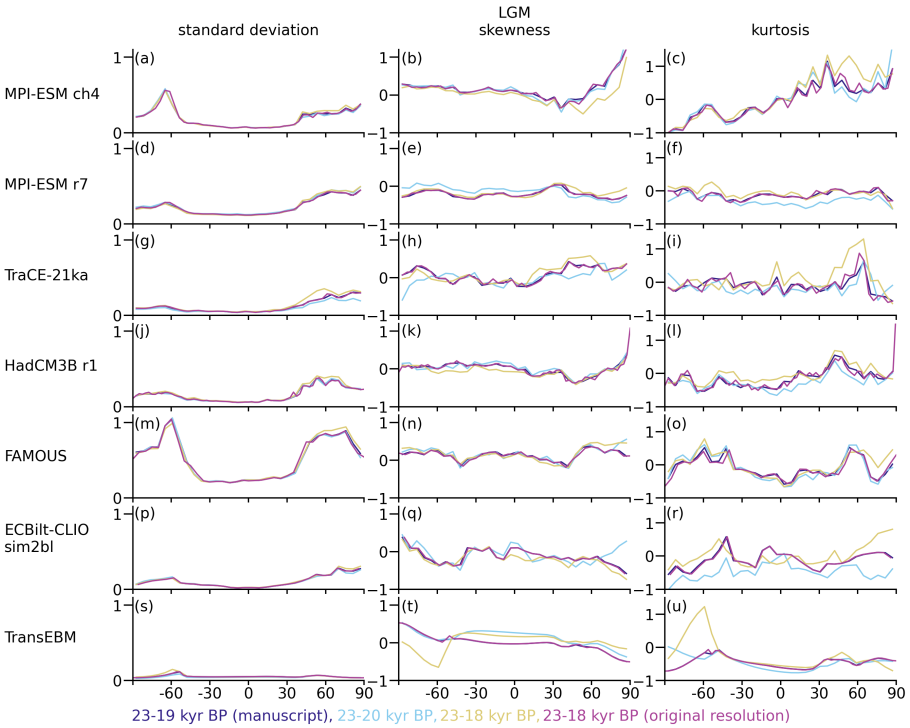

Figure S39. Centennial latitudinal moments during the LGM for different definitions of the LGM and without regridding. Shown are standard deviation (left column), skewness (middle column), kurtosis (right column) for all main set simulations. The version used in the manuscript is shown in dark blue. ECBilt-CLIO was at T21 resolution and thus did not require regridding. Therefore, for this simulation the versions marked "manuscript" and "original resolution" are identical.

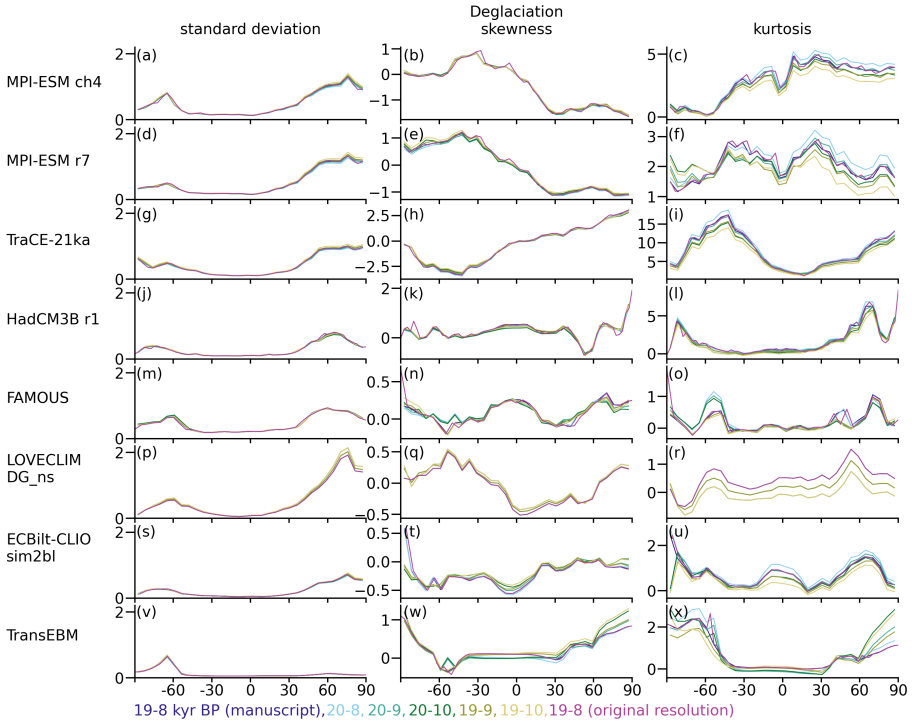

Figure S40. Centennial latitudinal moments during the Deglaciation for different definitions of the Deglaciation and without regridding. Shown are standard deviation (left column), skewness (middle column), kurtosis (right column) for all main set simulations. The version used in the manuscript is shown in dark blue. Note that since LOVECLIM DG_ns only starts at 19kyr, only those versions exist for this simulation. LOVECLIM DG_ns and ECBilt-CLIO were at T21 resolution and thus did not require regridding. Therefore, for them the versions marked "manuscript" and "original resolution" are identical.

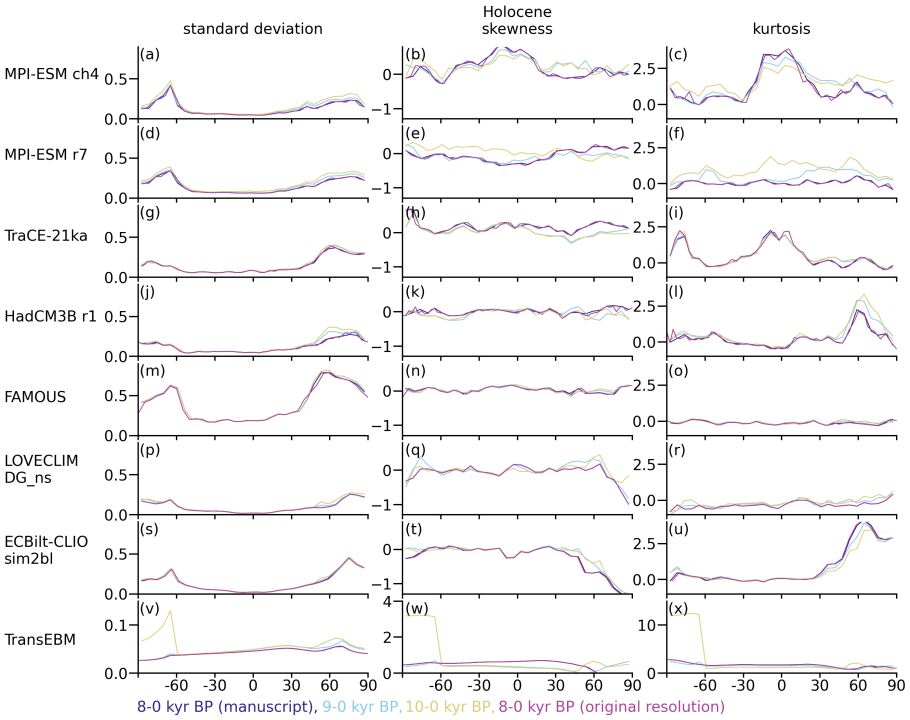

Figure S41. Centennial latitudinal moments during the Holocene for different definitions of the Holocene and without regridding. Shown are standard deviation (left column), skewness (middle column), kurtosis (right column) for all main set simulations. The version used in the manuscript is shown in dark blue. LOVECLIM DG_ns and ECBilt-CLIO were at T21 resolution and thus did not require regridding. Therefore, for them the versions marked "manuscript" and "original resolution" are identical.